

# A comparative study of eight human auditory models of monaural processing

Alejandro Osses Vecchi,<sup>1</sup> Léo Varnet,<sup>1</sup> Laurel H. Carney,<sup>2</sup> Torsten Dau,<sup>3</sup> Ian C. Bruce,<sup>4</sup> Sarah Verhulst,<sup>5</sup> and Piotr Majdak<sup>6</sup>

<sup>1</sup>*Laboratoire des systèmes perceptifs, Département d'études cognitives, École Normale Supérieure, PSL University, CNRS, Paris, France\**

<sup>2</sup>*Departments of Biomedical Engineering and Neuroscience, University of Rochester, Rochester, NY, USA*

<sup>3</sup>*Hearing Systems Section, Department of Health Technology, Technical University of Denmark, Lyngby, Denmark*

<sup>4</sup>*Department of Electrical and Computer Engineering, McMaster University, Hamilton, ON, Canada*

<sup>5</sup>*Hearing Technology group, WAVES, Department of Information Technology, Ghent University, Ghent, Belgium*

<sup>6</sup>*Acoustics Research Institute, Austrian Academy of Sciences, Vienna, Austria*

A number of auditory models have been developed using diverging approaches, either physiological or perceptual, but they share comparable stages of signal processing, as they are inspired by the same constitutive parts of the auditory system. We compare eight monaural models that are openly accessible in the Auditory Modelling Toolbox. We discuss the considerations required to make the model outputs comparable to each other, as well as the results for the following model processing stages or their equivalents: outer and middle ear, cochlear filter bank, inner hair cell, auditory nerve synapse, cochlear nucleus, and inferior colliculus. The discussion includes some practical considerations related to the use of monaural stages in binaural frameworks.

Pages: 1–20

## I. INTRODUCTION

Computational auditory models reflect our fundamental knowledge about hearing processes and have been accumulated during decades of research [e.g., 1]. Models are used to derive conclusions, reproduce findings, and develop future applications. Usually, models are build in stages that reflect basic parts of the auditory system, such as cochlear filtering, mechanoneural interface, and neural processing, by applying signal-processing methods such as bandpass filtering and envelope processing, among others [2]. Models of monaural processing often form a basis for binaural models [e.g., 3] and more complex models of auditory-based multimodal cognition [e.g., 4]. For this reason, combined with the increasing popularity of reproducible research [5], it is not surprising that there is an increasing number of auditory models available as software packages [e.g., 6–8].

However, models must be used with caution because they approximate auditory processes and are designed and evaluated under a specific configuration for a specific set of input sounds. While the evaluation conditions are selected to test the main properties of the simulated stages, models may provide different predictions when processing “unseen sounds.” Combined with the wide and low-threshold availability of model implementations, there is a chance of applying a model outside its specific signal or parameter range. Thus, studies comparing models’ properties and configurations are important to model users. For example, Saremi *et al.* [9] compared seven models of cochlear filtering with respect to various

parameters describing the nonlinear filtering process of an active cochlea, and Lopez-Poveda [10] compared eight models of the auditory periphery based on the reproduction of auditory-nerve properties. Most other related studies focus on a specific task [e.g., 11–13] or an introduction to modelling frameworks [14, 15].

In the current study, we compare various monaural auditory models that approximate subcortical neural processing. We provide insights into advantages and limitations, as well as into considerations that are relevant for binaural processing. While our comparison provides guidelines for model selection, we also provide model configurations that reduce the heterogeneity across model outputs. These configurations are evaluated using the same set of sound stimuli across models.

We analysed auditory models fulfilling two main criteria. First, the selected models describe the auditory path beginning with the acoustic input up to subcortical neural stages, in the cochlear nucleus (brainstem) and the inferior colliculus (midbrain). These neural processing stages are often used to simulate higher order processes such as speech encoding. Consideration of these stages extends previous comparisons of auditory periphery models [9, 10]. Second, the model implementations are publicly available and validated to simulate psychoacoustic performance and/or physiological properties. We use the implementations available in the Auditory Modelling Toolbox (AMT) [8, 16].

Based on our inclusion criteria, some models are excluded from the comparison, e.g., models that have only been evaluated at the level of cochlear filtering, such as models based on Hopf bifurcation [17] and the model of asymmetric resonators with fast-acting compression from [18]. Further, we did not include models focusing

\*) Electronic mail: ale.a.osses@gmail.com.

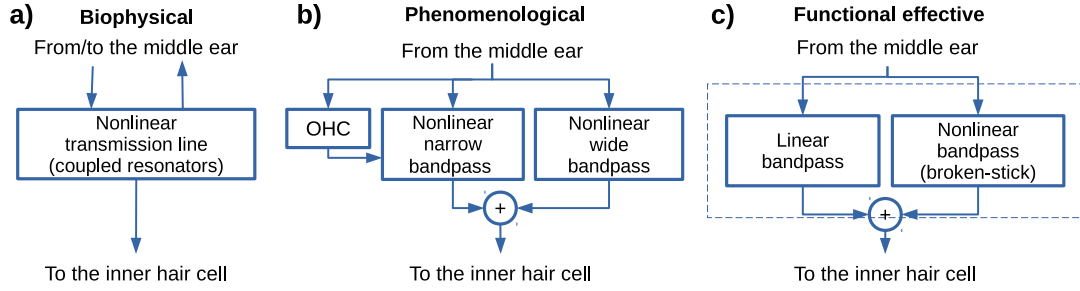


FIG. 1. Model families used in this study. The families are defined by the level of detail in simulating the cochlear processing and are sorted by their complexity from left to right. a) Biophysical models using a nonlinear transmission line consisting of resonating stages coupled by the cochlear fluid. b) Phenomenological models using nonlinear filters dynamically controlled by an outer-hair-cell (OHC) model. c) Functional effective models using static linear filters, optionally combined with static nonlinear filters.

on specific psychoacoustic metrics [19, 20], despite the fact that such models are often based on comparable auditory stages as those described in this study. Also, for the sake of simplicity, our analyses are focused on the comparison *across* models rather than on a comparison with experimental data. Nevertheless, we provide experimental references to the simulations that are illustrated throughout this paper. Additionally, to encourage reproducible research in auditory modelling, all our paper figures can be retrieved using AMT 1.0, including (raw) waveform representations of intermediate model outputs.

On the other hand, we provide insights relevant for the binaural system, including properties that can often be attributed to the effects of the monaural auditory processing, e.g., the temporal processing of interaural level differences [21]. To do so, the set of sounds and metrics used to evaluate the selected models were chosen to include fast and slow temporal aspects, such as temporal fine structure and temporal envelope, and to contain a wide range of presentation levels.

TABLE I. List of selected models. The model labels used in this study correspond with the model functions in AMT 1.0.

Label	Reference
dau1997	Dau <i>et al.</i> (1997) [22]
zilany2014	Zilany <i>et al.</i> (2014) [23] and Carney <i>et al.</i> (2015) [24]
verhulst2015	Verhulst <i>et al.</i> (2015) [25]
verhulst2018	Verhulst <i>et al.</i> (2018) [26]
bruce2018	Bruce <i>et al.</i> (2018) [27] and Carney <i>et al.</i> (2015) [24]
king2019	King <i>et al.</i> (2019) [28]
relanoiborra2019	Relaño-Iborra <i>et al.</i> (2019) [29]
osses2021	Osses & Kohlrausch (2021) [30]

## II. MODELS

We define three model families, classified by their objectives [31], which translate into three different levels of detail in simulating the cochlear processing, as schema-

tised in Fig. 1. The selected models are listed in Table I and are labelled throughout this paper by the last name of the first author and the year of the corresponding publication. This naming system directly reflects the corresponding model functions implemented in AMT 1.0 [8].

We define the family of *biophysical models* (Fig. 1a) that use a transmission line consisting of many resonant stages coupled by the cochlear fluid. Biophysical models aim at exploring how the properties of the system emerge from biological-level mechanisms, needing a fine-grained description at this level. The biophysical models are represented by verhulst2015 [25] and its extended version, verhulst2018 [26] (model version 1.2 [32, 33]). We further define *phenomenological models* which are primarily concerned with predicting physiological properties of the system, using a more abstract level of detail than the biophysical models. The phenomenological models considered here rely on dynamically adapted bandpass-filtering stages combined with nonlinear mappings (Fig. 1b) and are represented by zilany2014 [23] and its extended version bruce2018 [27], both combined with the same-frequency inhibition-excitation (SFIE) stages for subcortical processing [34]. Further approximation is given by *functional-effective models* [35], which target the simulation of behavioural (perceptual) performance rather than the direct simulation of neural representations, and usually approximate the cochlear processing by using static bandpass filtering with an optional nonlinear mapping (Fig. 1c). The linear effective models are represented by dau1997 [22] and osses2021 [30] and the nonlinear effective models are represented by king2019 [28] and relanoiborra2019 [29]. Given that for each model a similar level of approximation has been generally used in the design of subsequent model stages, we use the described classification to reflect the nature of the entire model, from cochlear processing to the processing of higher stages.

The selected monaural models share common stages of signal processing, as indicated in the schematic diagrams of Fig. 2. Each model stage mimics, with greater or lesser detail, underlying hearing processes along the

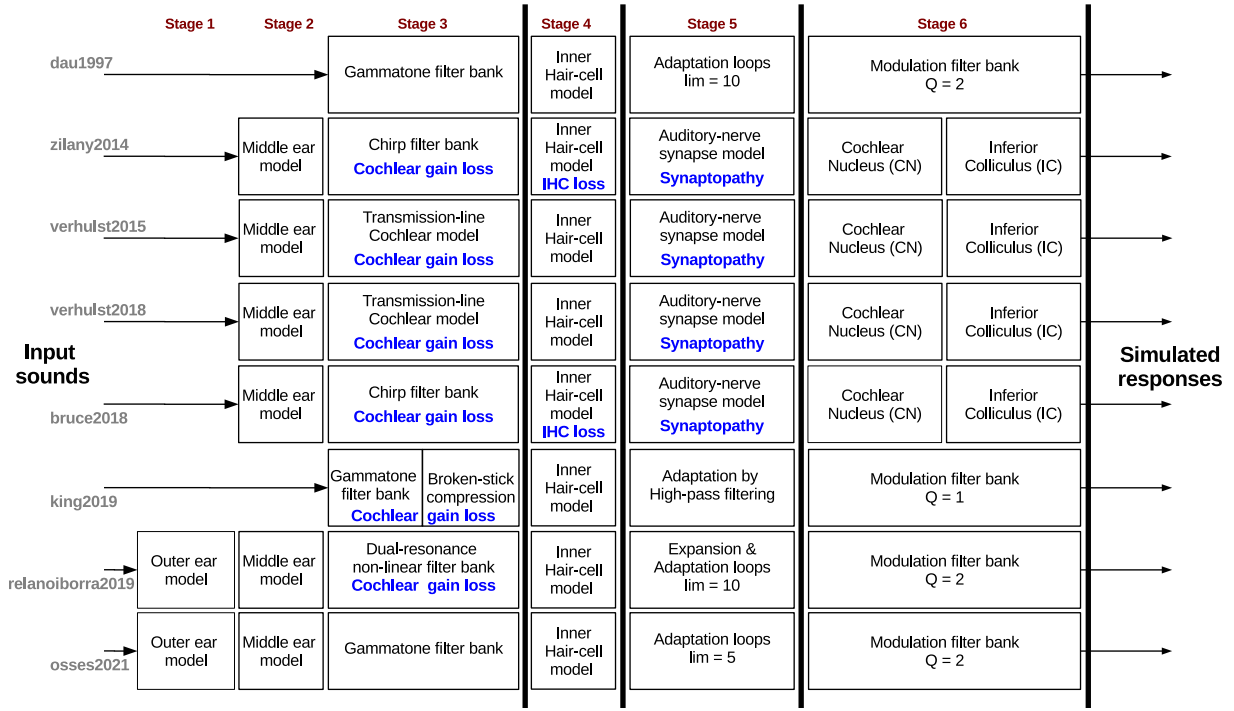


FIG. 2. Block diagrams of the selected auditory models. Vertical lines: Intermediate model outputs as the basis for the evaluation in the corresponding sections. Blue: Type of hearing impairment that can be accounted for in the corresponding stage (see a brief overview in Sec. V A).

ascending auditory pathway. The thick vertical lines in Fig. 2 indicate the intermediate model outputs which are the basis for our evaluation. Note that these stages are, conceptually speaking, independent of each other, however because of nonlinear interactions between them, processing performed by these stages is not commutative, thus requires a step-by-step approach. Next, we provide a brief description of each model stage.

### A. Outer ear

The listener’s head, torso, and pinna filter incoming sounds. The ear-canal resonance further emphasises frequencies around 3000 Hz [36]. Both effects can be accounted for by filtering the sound with a head-related transfer function [e.g., 37] and then applying a headphone-to-tympanic-membrane transfer function, as used in relanoiborra2019 and osses2021. The other six selected models do not include an outer-ear filter, implicitly assuming that either the outer ear does not introduce a significant effect in the subsequent sound processing chain, or that the sounds are presented near the tympanic membrane, as is the case for a sound presentation using in-ear earphones.

### B. Middle ear

Six of the eight evaluated models include a stage of middle-ear filtering. The transfer functions of the middle-ear filters used in these models are shown in Fig. 3. The

transfer functions have been designed to represent stapes velocity near the oval window of the cochlea. The verhulst2015 and verhulst2018 models use an approximation of middle-ear forward pressure gain (“M1” in [38]). The humanised zilany2014 and bruce2018 models use a linear middle-ear filter [39, 40] designed to match experimental data [41]. The relanoiborra2019 model uses the filter from [42, 43]. The osses2021 model also uses the filter from [42, 43] scaled to provide a 0-dB amplitude in the frequency range of the passband and a fixed group-delay compensation.

Middle-ear filtering not only introduces a bandpass characteristic to the incoming signal (Fig. 3), but also affects the operating range of cochlear compression in models relying on nonlinear cochlear processing, i.e., verhulst2015, verhulst2018, zilany2014, bruce2018, and relanoiborra2019. The passband gains of the middle-ear filters are indicated in Table II and range between  $-66.9$  dB (relanoiborra2019) and  $+24$  dB (verhulst2015). In nonlinear models, lower and higher passband gains vary the actual input level to the filter bank, shifting the start of the compression to higher and lower knee points, respectively.

### C. Cochlear filtering

A cochlear filter bank performs a spectral analysis of incoming signals by simulating the mechanical oscillations of the basilar membrane (BM) in the cochlea. Because of complex interactions between the BM, the

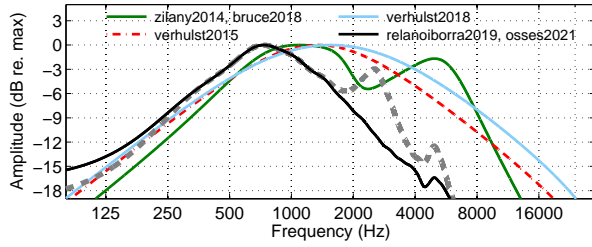


FIG. 3. Amplitude spectra of the four middle-ear filters used in six of the evaluated models. The lines were shifted vertically to display their individual maximum at 0 dB. For *relanoiborra2019* and *osses2021*, the grey dashed line shows the combined response of the outer- and middle-ear filters.

cochlear fluid, and outer hair cells (OHCs), this analysis depends on the tonotopic position along the cochlea. All approaches used to simulate cochlear filtering produce a set of  $N$  temporal signals, for  $N$  simulated characteristic frequencies (CFs). Each cochlear section, having a CF expressed in Hz, is assumed to either have relatively sharp frequency tuning [44]:

$$Q_{\text{ERB}} = 12.7 \cdot (\text{CF}/1000)^{0.3} \quad (1)$$

or broader tuning [45]:

$$Q_{\text{ERB}} = \text{CF} / [24.7 \cdot (4.37 \cdot \text{CF}/1000 + 1)] \quad (2)$$

In *verhulst2015* and *verhulst2018*, the cochlear filtering is simulated by a transmission-line model [46]. In *zilany2014* and *bruce2018*, the filtering is based on a chirp filter bank [47] tuned to a human cochlea [39, 40, 48]. In these models, the cochlear filters are assumed to be tuned according to Eq. 1.

In *dau1997* and *osses2021*, the linear Gammatone filter bank from [49] is used. *King2019* uses the Gammatone filter bank from [49] followed by a compressive stage acting above a given knee point. In *relanoiborra2019*, the cochlear processing is simulated by the dual-resonance nonlinear filter bank (DRNL) [42]. The cochlear filters of these models are assumed to be tuned according to Eq. 2.

#### D. Inner hair cell

The inner hair cells (IHCs) transform the mechanical BM oscillations into receptor potentials, subsequently initiating neuronal discharges in the auditory nerve (AN) [50]. In the most simple approach, the IHC processing can be simulated as an envelope detector that removes phase information for high CFs, implemented as a half-wave rectification followed by a lowpass (LP) filter. This approach is used in *dau1997*, *king2019*, *relanoiborra2019*, and *osses2021*, in which the LP filters have  $-3$ -dB cut-off frequencies ( $f_{\text{cut-off}}$ ) between 1000 and 2000 Hz. In *zilany2014*, *bruce2018*, and *verhulst2015*, a nonlinear transformation is applied to the output of the cochlear filter bank, followed by a cascade of LP filters with  $f_{\text{cut-off}}$  of 3000 Hz (*zilany2014* and *bruce2018*)

and 1000 Hz (*verhulst2015*). The resulting  $f_{\text{cut-off}}$  of each model ranges between 642 Hz (*verhulst2015*) and 1000 Hz (*dau1997*, *relanoiborra2019*, *king2019*), as indicated in Table II. In *verhulst2018*, a more sophisticated IHC model is used [51], that is implemented as a three-channel Hodgkin-Huxley type model, with each of the channels representing mechanoelectrical and (fast and slow) potassium-gated processing [26, 51].

#### E. Auditory nerve

The transduction from receptor potentials into patterns of neural activity can be derived from the interaction between the IHC and AN. Several AN synapse models have been inspired by the three-store diffusion model [50], assuming that the release of synaptic material is managed in three storage compartments. For steady-sound inputs, this model predicts a rapid neural firing shortly after the sound onset with a decreasing rate towards a plateau discharge rate, a phenomenon called adaptation.

The AN synapse models in *verhulst2015*, *verhulst2018*, and *zilany2014* are based on [50], but *zilany2014* further incorporates a power-law adaptation following the diffusion model from [23]. The synapse model in *bruce2018* uses a diffusion model based on [52] to: (1) have limited release sites, and (2) come after the power-law adaptation instead of before it [27]. The outputs of these models simulate the firing of neuron synapses<sup>1</sup> having a specific spontaneous rate of high-, medium-, and/or low-spontaneous rates.

The effective models, on the other hand, rely on a more coarse AN simulation, expressed in arbitrary units (a.u.). In *king2019*, adaptation is simulated by applying a highpass filter with a cut-off frequency of 3 Hz [28]. In *dau1997*, *relanoiborra2019*, and *osses2021*, adaptation is simulated by so-called adaptation loops [35] that introduce a nearly logarithmic compression to stationary input signals and a linear transformation for fast signal fluctuations (Appendix B in [30]). The arbitrary units of these transformed outputs are named model units (MUs).

#### F. Subcortical processing

AN firing patterns propagate to higher stages along the auditory pathway, first through the auditory brainstem, then towards more cortical regions [53]. On its way, AN spiking is mapped onto fluctuation patterns by neurons that are sensitive to the amplitude of low-frequency fluctuations [54]. This fluctuation sensitivity has been approximated using various approaches. Our analyses focus on model approximations of the ventral cochlear nucleus (CN) and inferior colliculus (IC) [34], as well as on different modulation-filter-bank variants [22, 55]. As a result, we exclude the analysis of other subcortical structures such as those that play a particular role in the bin-aural interaction between ears (e.g., the dorsal cochlear nucleus and lateral superior olive) [53, 56].



The processing in the ventral CN and IC can be simulated using the same-frequency inhibition-excitation (SFIE) model, resulting in a widely tuned modulation filter (Q factor  $\approx 1$ ) with a best-modulation frequency (BMF) depending on the parameters of the model [24, 34]. The SFIE model has already been used in combination with the biophysical and phenomenological models described here. For example, zilany2014 has been combined with the SFIE model using between one and three modulation filters [e.g., 57]. Or, verhulst2015 and verhulst2018 have been combined with the SFIE model tuned to one modulation filter centred at a BMF of 82.4 Hz (see Table II) [26, 32]. Further, bruce2018 can be combined with the SFIE model in the UR EAR 2020b toolbox [58]. Note that zilany2014, verhulst2015, and verhulst2018 have used the output of their mean firing rate generator –an output that can be conceptualised as peristimulus time histograms (PSTHs) [59]– as an input to the SFIE model. In bruce2018, because of the stochastic processes in its spike generator, repeated processing of the same stimulus is recommended to obtain a faithful PSTH that can appropriately account for power-law adaptation properties (see Sec. 3 in [27]).

In the effective models, on the other hand, subcortical neural processing is further approximated based on the modulation-filter-bank concept [22, 55]. In dau1997, king2019, relanoiborra2019, and osses2021, linear modulation filter banks are used, covering a range of BMFs up to 1000 Hz. In dau1997, twelve modulation filters with a Q-factor of 2 and overlapped at their  $-3$  dB points are used. The same modulation filters are used in relanoiborra2019 and osses2021, but an additional 150-Hz LP filter is applied [60] and the number of filters is limited so that the highest BMF is less than a quarter of the corresponding CF [61]. In king2019, the filter bank is used with a wider tuning (Q=1), using ten 50%-overlapped filters having a maximum BMF of 120 Hz [28].

### III. MODEL CONFIGURATION

We evaluated the intermediate model outputs that are indicated by thick vertical black lines in Fig. 2. The evaluation points are located after the cochlear filter bank (Stage 3), the IHC processing stage (Stage 4), the AN synapse stage or equivalent (Stage 5), and after the IC processing stage or equivalent (Stage 6). Starting with the default parameters of each model, we introduced small adjustments to obtain the most comparable model outputs. All the comparisons can be reproduced with the function `exp_osses2022` from AMT 1.0 [8].

#### A. Level scaling

The same set of sound stimuli was used as input to all models. The waveform amplitudes were assumed to represent sound pressure expressed in Pascals (Pa). The models zilany2014, verhulst2015, verhulst2018, bruce2018, and relanoiborra2019 use this level convention and did not require further level scaling. The models dau1997,

king2019, and osses2021 interpret sound pressures between  $-1$  and  $1$  Pa as amplitudes in the range  $\pm 0.5$ , thus a factor of 0.5 (attenuation by 6 dB) was applied to the generated stimuli to meet the level convention of these models. For these latter models, which include mostly level-independent stages, such calibration is relevant because the adaptation loops (used in dau1997, osses2021, also extensible to relanoiborra2019) include level-dependent scaling (Eqs. B1–B3 in [30]). In king2019 a calibrated knee point (default of 30 dB) is used in its cochlear compression stage (Stage 3). All signal levels are reported as root-mean-square (rms) values referenced to  $20 \mu\text{Pa}$ , in dB sound pressure level (dB SPL).

#### B. Cochlear filtering

The phenomenological and effective models can be set to simulate any CF. The biophysical models, however, because of the nature of the transmission-line structure, have a discrete tonotopy that translates into a discrete set of available CFs.

The models verhulst2015 and verhulst2018 were set to 401 cochlear sections spaced at  $\Delta x = 0.068$  mm with tonotopic distances  $x_n$  ranging between  $x_1 = 3.74$  mm and  $x_{401} = 30.9$  mm, that are related to CFs between  $\text{CF}_1 = 12010$  Hz and  $\text{CF}_{401} = 113$  Hz, according to the apex-to-base mapping of Eq. 3 [62],

$$\text{CF}_n = A_0 \cdot \left( 10^{-a \cdot x_n / 1000} \right) - A \cdot k \quad (3)$$

where  $x_n$  (in mm) can be obtained as  $x_1 + \Delta x \cdot (n - 1)$ , and  $A = 165.4188$  Hz,  $a = 61.765$  1/m,  $k = 0.85$ , and  $A_0 = 20682$  Hz. Note that when reporting results, we indicate the cochlear section number  $n$  and its corresponding  $\text{CF}_n$ .

The cochlear-filtering parameters of zilany2014 and bruce2018 were those adapted to a human cochlea [39, 40]. Moreover, in order to analyse separately the effects of cochlear filtering and IHC processing in zilany2014, the outputs from the chirp filters representing the static and OHC-controlled filters (C2 and C1 in [23]) were added together and analysed before the IHC nonlinear mapping was applied. This analysis follows a similar rationale as analysing the main output of the DRNL filter bank in relanoiborra2019 (see Fig. 3a from [42]).

Finally, in king2019, we used a compression factor of 0.3 for all simulated CFs, which is different from the one-channel (on-CF) compression used in [28].

#### C. Inner hair cell and auditory nerve

Default parameters were used for the IHC and AN stages of the evaluated effective models. However, the biophysical and phenomenological models require the choice of parameters to simulate a population of AN fibres. For each CF we simulated 20 fibres, having either high- (HSR), medium- (MSR), or low-spontaneous rates (LSR), distributed in percentages of 60-20-20% [63, 64], resulting in a 12-4-4 configuration (HSR-MSR-LSR).

Note that for `verhulst2015` and `verhulst2018`, this deviates from the standard 13-3-3 configuration [25, 26]. For `verhulst2015` and `verhulst2018`, the spontaneous rates of each fibre type were 68.5, 10, and 1 spikes/s for HSR, MSR, and LSR, respectively, as used in human-tuned simulations [26]. For `zilany2014`, the spontaneous rates of each fibre type were 100, 4, and 0.1 spikes/s and for `bruce2018` were 70, 4, and 0.1 spikes/s for HSR, MSR, and LSR, respectively. We further disabled the random fractional noise generators in `zilany2014` and `bruce2018` [65], and the random spontaneous rates in `bruce2018` (“std” from Tab. I in [27] was set to zero). With this configuration, the mean-rate synapse outputs of `verhulst2015`, `verhulst2018`, `zilany2014`, and `bruce2018` are deterministic. For this reason, to obtain population responses, we simulated the AN processing of each type of neuron only once and then weighted them by factors of 0.6, 0.2, and 0.2 for HSR, MSR, and LSR fibres, respectively. In contrast, the PSTH outputs that are reported for `zilany2014` and `bruce2018` are not deterministic, requiring the simulation of each AN fibre for each CF. Therefore, PSTH population responses were obtained by counting the average number of spikes in time windows of 0.5 ms across 100 repetitions of the corresponding stimuli.

#### D. Subcortical processing

The default configuration of the model stages of subcortical processing (Stage 6, Fig. 2) differs in the number of modulation filters (from 1 to 12) and in their tuning across models. In our study, we use only one modulation filter targeting a BMF of approximately 80 Hz (see “Theoretical BMF” in Table II) and a Q-factor of approximately 1 for `zilany2014`, `verhulst2015`, `verhulst2018`, `bruce2018`, and `king2019`, and a Q-factor of 2 for `dau1997`, `relanoiborra2019`, and `osses2021`.

For the biophysical and phenomenological models, we used the SFIE model [24, 34] using two different configurations. The SFIE model [34] integrated in `verhulst2015` and `verhulst2018` has CN parameters with excitatory and inhibitory time constants of  $\tau_{\text{exc}} = 0.5$  ms and  $\tau_{\text{inh}} = 2$  ms, a delay  $D = 1$  ms, and a strength of inhibition of  $S = 0.6$ . The IC stage uses  $\tau_{\text{exc}} = 0.5$  ms,  $\tau_{\text{inh}} = 2$  ms [26],  $D = 2$  ms, and  $S = 1.5$  [34], achieving a BMF of 82.4 Hz.

For `zilany2014` and `bruce2018`, the SFIE model is a separate stage [24], implemented as `carney2015` in AMT 1.0, where either the mean-rate (`zilany2014`) or the PSTH outputs (`bruce2018`) are used as inputs. In our analysis, we only used the output of the band-enhanced IC cell, which corresponds to the SFIE model from [34]. The CN parameters were identical to those for the biophysical models. The IC parameters were  $\tau_{\text{exc}} = 1.11$  ms,  $\tau_{\text{inh}} = 1.67$  ms,  $D = 1.1$  ms, and  $S = 0.9$ , achieving a BMF of 83.9 Hz [24]. Note the different inhibition strength  $S$  between models. In the biophysical models, the IC output is dominated by inhibitory responses ( $S > 1$ ) whereas in the phenomenological models the IC output is dominated by excitatory responses ( $S < 1$ ).

## IV. EVALUATION

In this section we analyse the outputs of the eight selected auditory models in a number of test conditions, whose results are presented in Figs. 4–14. We aimed at a comparison across models and thus, for the sake of clarity, we refrained from a direct comparison to ground-truth references from physiological data. However, such a comparison is important and interesting. For this reason, we provide references where similar experimental and/or simulation analyses have been presented. These references are indicated as “Literature” in the caption of the corresponding figure. Alternatively, the outputs of the biophysical and phenomenological models may be considered as referential because they have been primarily developed to reflect physiological responses to sounds.

### A. Cochlear filtering: Compressive growth

Sound processing in the cochlea depends not only on the frequency but also on the level of the input stimulus. The amplitude of the vibration displacement increases for higher levels, following an amplitude growth that comprises linear and compressive regimes [66]. For this reason, we assessed the curve relating the input stimulus levels with levels at the output of the filter banks, known as input-output (I/O) curves for (1) the on-frequency CF tuned to the frequency of the input stimulus, and (2) the off-frequency responses of cochlear filters tuned to one equivalent rectangular bandwidth number ( $\text{ERB}_N$ ) [45] below and above the stimulus frequency. We report the I/O curves for pure tones of frequencies 500 and 4000 Hz, with a duration of 100 ms, presented at levels between 0 and 100 dB SPL (steps of 10 dB), gated on and off with a 10-ms raised-cosine ramp.

The obtained I/O curves are shown in Fig. 4 for on-frequency (left panels) and off-frequency simulations ( $\pm 1 \text{ ERB}_N$ , middle and right panels). Note that the I/O curves were vertically shifted by the reference gains provided in Table II which were derived for each model for a pure tone of frequency 1000 Hz and 100 dB SPL. As expected for the level-independent Gammatone filters used in `dau1997` and `osses2021`, the curves were linear in all panels of Fig. 4. For the remaining models, more compressive behaviour was observed for on-frequency curves (left panels) while more linear curves were obtained for off-frequency CFs (middle and right panels), except for `relanoiborra2019` and `king2019`, that had on- and off-frequency compression.

For `zilany2014`/`bruce2018`, the I/O curves were fairly linear in response to 500-Hz tones (top panels) for both on- and off-frequency CFs. For 4000-Hz tones, a prominent compressive behaviour was observed in the on-frequency curves (panel d) where, additionally, the curve for `verhulst2018` turned from a compressive to a linear regime for signal levels above 80 dB. The off-frequency I/O curves obtained for `verhulst2018` were similar to those for `verhulst2015` but had overall lower and higher amplitudes for the pure tones of 500 Hz (panels b–c) and

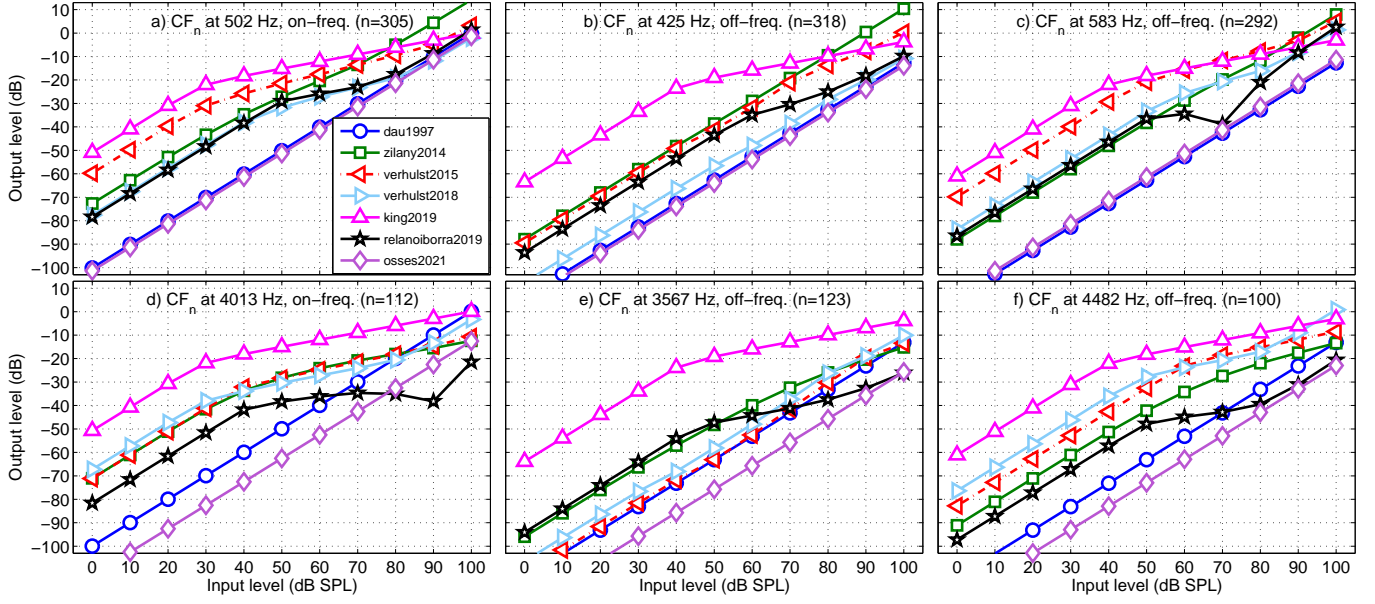


FIG. 4. Input-output (I/O) curves for pure tones. **Top (a–c):** Stimulus frequency of 500 Hz. **Bottom (d–f):** Stimulus frequency of 4000 Hz. **Left (a,d):** On-frequency simulations, i.e., output of the cochlear filter with the CF tuned to that of the stimulus frequency. **Middle (b,e), right (c,f):** Off-frequency simulations, one ERB below and above the on-frequency, respectively. The exact simulated on- and off-frequency CFs are indicated in the title of each panel. All I/O curves were shifted vertically by the reference gains given in Table II (see the text for details). **Literature:** Figs. 1–3 from [66] and Fig. 3 from [9].

4000 Hz (panels e–f), respectively, as a consequence of the differences in their middle-ear filters (see Fig. 3). The tendency to a more linear regime in off-frequency CFs has been shown previously [66]. This is in fact the basis for having compression only applied to the on-frequency channel in king2019 [28]. However, the default compression rate of 0.3 for the on-frequency channel with no compression for off-frequency channels leads to an unrealistic level balance between on- and off-frequency channels.

## B. Cochlear filtering: Frequency selectivity

The frequency selectivity of each filter bank was computed in response to Gaussian noises with a flat spectrum between 20 and 10000 Hz, presented at 40, 70, and 100 dB SPL. Due to the stochasticity of these stimuli, we obtained model responses to a 3-s long noise that were subsequently analysed and averaged in the frequency domain using 500-ms sections. The same 3-s noise was used for all test levels, after the corresponding level scaling.

### a. Filter tuning.

The frequency response of thirty-two filters with CFs between 126 Hz ( $n = 396$ ) and 9587 Hz ( $n = 24$ , Eq. 3) at steps of  $n = 12$  bins was obtained. For each filter response, a quality factor  $Q_{-3\text{ dB}} = \text{CF}/\text{BW}$  was obtained, where BW is the bandwidth defined by the lower and upper 3-dB down points of each filter transfer function.

The frequency selectivity simulations for each of the filter banks are shown in Fig. 5 for the noises at 40 (panel a), 70 (panel b), and 100 dB SPL (panel c). The an-

alytical filter tuning curves given by Eqs. 1 and 2 are indicated as light and dark grey traces in Fig. 5. Note that with this comparison we assume that the Q factors within one ERB are similar to  $Q_{-3\text{ dB}}$  values. The results for 40-dB noises show that the frequency selectivity follows either the analytical tuning of Eq. 1 (zilany2014, bruce2018, verhulst2015, and verhulst2018) or the tuning of Eq. 2 (dau1997, relanoiborra2019, king2019, and osses2021). When looking at the results for higher levels (Fig. 5b–c), no change in tuning was observed for dau1997 and osses2021, as expected for linear models with no compression. For the nonlinear models, the results in Fig. 5b for 70-dB noises showed overall lower Q factors, but with only a small change for king2019 and relanoiborra2019. The results for 100-dB noises in Fig. 5c showed a further lowering of Q factors in the biophysical and phenomenological models, reaching values as low as  $Q \approx 2$  in verhulst2015, lower Q factors for frequencies up to about 4000 Hz in relanoiborra2019, and virtually unaffected Q factors in king2019. A closer inspection to the outputs of king2019 revealed that there was a filter broadening as a consequence of its broken-stick nonlinearity stage, but this broadening predominantly affected the frequency responses outside the range defined by the 3-dB bandwidth used to derive the Q factors. To illustrate the Q-factor transition when increasing the signal level in each model, the difference between Q factors obtained from 40- and 100-dB noises is shown in Fig. 5d, where a decrease in Q factor with increasing signal level is represented by a positive Q difference.



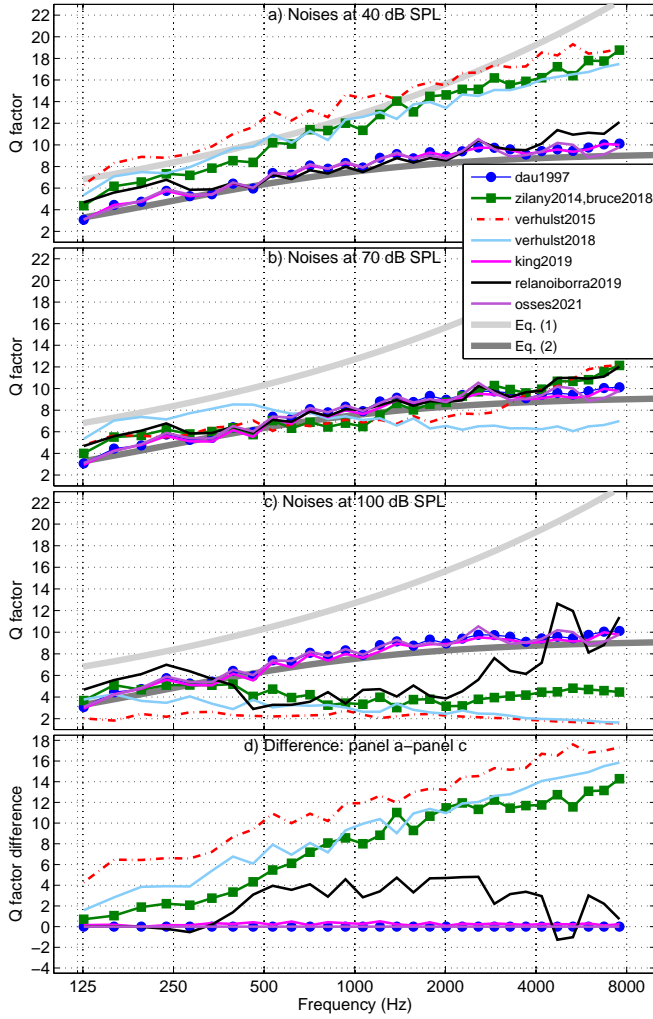


FIG. 5. Filter tuning expressed as quality factors  $Q$  for noises of 40, 70, and 100 dB SPL (panels **a-c**), and  $Q$ -factor difference obtained from the results of 40- and 100-dB noises (panel **d**). **Literature:** Fig. 4 from [44] and Fig. 4B from [9].

Additionally, we observed that *relanoiborra2019* and *king2019* introduce a change in selectivity at overall higher levels compared to the biophysical and phenomenological models. A closer look at this aspect revealed that this change occurs because *relanoiborra2019* and *king2019* only apply compression after the bandpass filtering and, therefore, lower level signals are used as input for their compression (broken-stick) module.

#### b. Number of filters.

The number of filters in a filter bank is relevant for several model applications because too few filters can lead to a loss of signal information [e.g., 69] and too many filters may unnecessarily increase the computational costs. The number of filters is a free parameter in *zilany2014/bruce2018*, but is fixed for *verhulst2015* and *verhulst2018* to yield an accurate precision of the transmission-line solver [70]. The remaining models use by default one ERB-wide bands (*dau1997*,

*king2019*, and *osses2021*), or have an overlap every 0.5 ERB (*relanoiborra2019*).

Here, we report the minimum number of filters that are required to obtain a filter bank with overlapping at  $-3$ -dB points of the individual filter responses. Using the empirical  $Q$ -factors of Fig. 5, we assessed the number of filters that would be required to cover a frequency range between 126 Hz (bin  $n = 396$ , Eq. 3) and the first filter with its upper cut-off frequency equal or greater than 8000 Hz. The number of filters derived from the 40-dB and 100-dB frequency tuning curves (Fig. 5a,c) are shown in Table II, including the average filter bandwidth in ERB for the corresponding model.

For the biophysical models, the filters were much wider at the higher level than for the other models, with average bandwidths being as wide as 3.05 ERB for *verhulst2015* and 2.30 ERB for *verhulst2018*. This contrasts with the 1.57 ERB for *zilany2014* and *bruce2018* and the 1.15 ERB or less for the remaining models. These bandwidths are a consequence of the fast-acting (sample-by-sample) compression that is applied just before the transmission-line in the biophysical models and the slower-acting bandwidth control in *zilany2014* (denoted as the “control path” in the chirp-filter bank). While cochlear filters are generally wider at high sound levels [e.g., 71, 72], the appropriate tuning must be evaluated depending on the species’ characteristics, the tested CFs, and the type of evaluated excitation signals.

#### C. IHC processing: Phase locking to temporal fine structure

To illustrate the loss in phase locking to temporal fine structure with increasing stimulus frequency, we simulated IHC responses to pure tones with frequencies between 150 Hz ( $n = 387$ ) and 4013 Hz ( $n = 112$ , Eq. 3) spaced at  $n = 25$  bins, resulting in twelve test frequencies. The tones were generated at 80 dB SPL, with a duration of 100 ms, and were gated on and off with 5-ms raised-cosine ramps. The simulated waveforms, that are assumed to approximate the IHC potential, are displayed and described in terms of AC (fast-varying) and DC (average bias) components, and the simulated resting potentials ( $V_{\text{rest}}$ ). The AC potential was assessed from the peak-to-peak amplitudes as  $V_{\text{AC}} = V_{\text{peak,max}} - V_{\text{peak,min}}$ . The DC potential was obtained as  $V_{\text{DC}} = V_{\text{AC}}/2 - V_{\text{rest}}$  [67, 68].

The obtained IHC waveforms are shown in Fig. 6. Within each panel, bottom to top waveforms represent on-frequency simulations for the test signals, from low to high frequency carriers, respectively. For all model outputs, the four highest carriers ( $1870 \leq f_c \leq 4013$  Hz) were amplified by factors between 1 and 3, as indicated in the figure insets. The simulated voltages before the tone onset, i.e., the resting potential  $V_{\text{rest}}$ , were equal to 0 for all models except for *verhulst2018*, where  $V_{\text{rest}}$  was  $-57.7$  mV (not schematised in Fig. 6). It seems clear, however, that the decrease of peak-to-peak AC voltage available towards high frequencies –a measure of the residual amount temporal fine structure– is sig-



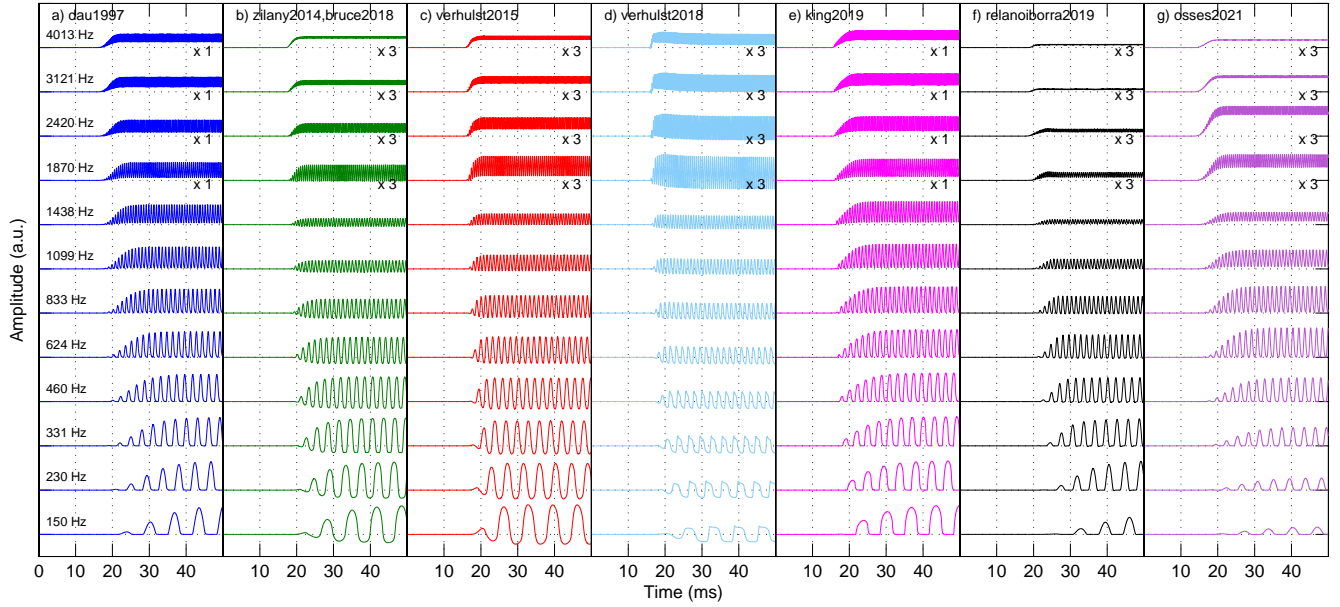


FIG. 6. Simulated IHC responses to pure tones of different frequencies evaluated at the corresponding on-frequency bin. The amplitudes were normalised with respect to their maximum value to allow a direct comparison across models. **Literature:** Fig. 9 from [67] and Fig. 7 from [68].

nificantly different across models. When increasing the CFs from 1099 to 4013 Hz, three models showed  $V_{AC}$  reduced by less than 76.0% (king2019: 59.7%, decreased from  $3.12 \cdot 10^{-3}$  to  $1.26 \cdot 10^{-3}$  a.u.; dau1997: 62.6%, decreased from 0.097 to 0.037 a.u.; and verhulst2018: 76.0%, decreased from 39.2 to 9.4 mV), while the other five models showed  $V_{AC}$  reductions of at least 92.5%. From the low-frequency IHC waveforms (bottom-most waveforms in each panel), it can be seen that the simulated amplitudes of dau1997, king2019, relanoiborra2019, and osses2021 did not go below their  $V_{rest}$  (horizontal grid lines in Fig. 6) as a result of the applied half-wave rectification process. Furthermore, zilany2014/bruce2018 and verhulst2015 have  $V_{peak,min}$  amplitudes of  $-66$  mV and  $-4.7$  mV, respectively. Despite the different range in their minimum voltages, there is a strong qualitative resemblance between waveforms (green and red traces in the figure). In fact both models use the same type of IHC nonlinearity (compare Eqs. 17–18 from [47] with Eqs. 4–5 from [25]). In these two models also the same LP filter implementation was used, only differing by the filter order and cut-off frequencies (see Table II).

The obtained AC/DC ratios are shown in Fig. 7, where a reduction in phase locking is related to a lower ratio. For all models, the ratio decreased with increasing frequency. All AC/DC curves, except that for verhulst2018, overlap well at low frequencies with ratios between 2.1 and 5.9 (below 1000 Hz), decreasing to ratios between 0.06 (osses2021) and 0.83 (dau1997) at 4013 Hz. Although the AC/DC curve for verhulst2018 showed the highest values (ratios between 137.4 at 460 Hz down to 1.3 at 4013 Hz), we still observed the systematic decrease in ratio with increasing frequency. If we further focus

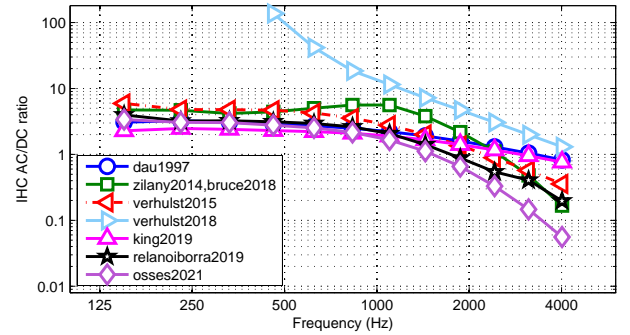


FIG. 7. Ratio between simulated AC and DC components ( $V_{AC}/V_{DC}$ , see the text) in response to 80-dB pure tones. **Literature:** Fig. 10 from [67] and Fig. 8 from [68].

on the AC/DC curves in the frequency range between 600 and 1000 Hz, where the phase-locking is expected to start declining [67], all models showed monotonically decreasing curves starting from about 833 Hz (except for verhulst2018, that always showed a decreasing tendency). The lowest ratios were observed for osses2021, followed by the similarly-steeped curve of zilany2014. Finally, a similar AC/DC curve was obtained for relanoiborra2019 and verhulst2015.

#### D. AN firing patterns

AN responses for a number of pure tones were simulated, including rate-level functions expressed as onset and steady-state responses, and the model responses to amplitude modulated (AM) tones. With these bench-

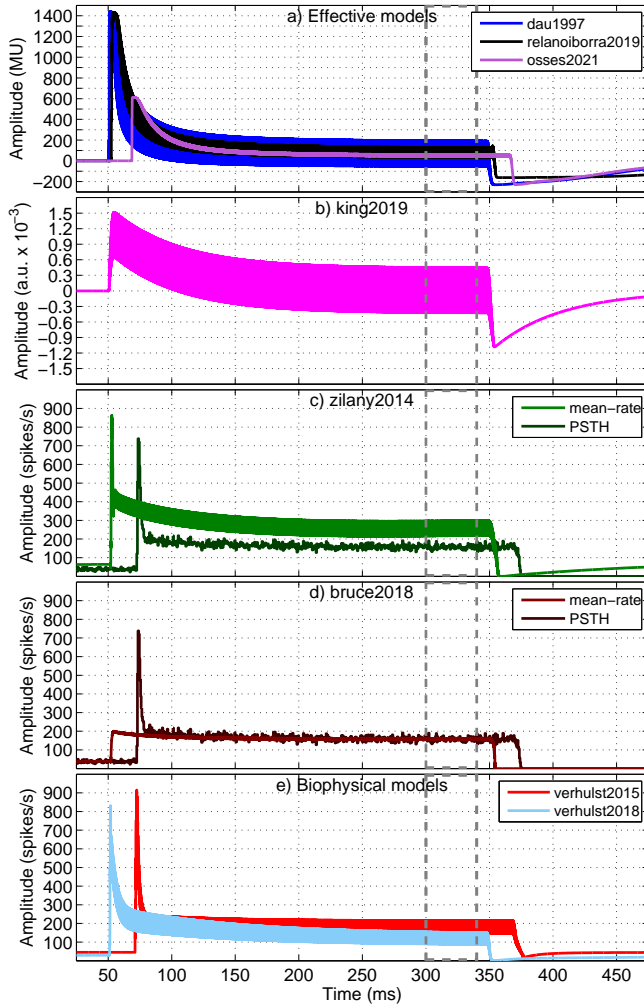


FIG. 8. Simulated AN responses to a 4000-Hz pure tone of 70 dB SPL. For ease of visualisation, the responses from osses2021, verhulst2015, and the PSTHs are horizontally shifted by 20 ms. **Literature:** Fig. 1 from [74] and Figs. 3 and 10 from [27].

marks we attempt to characterise the model responses at the output of the AN synapse stage or their equivalent, with a particular interest on the phenomenon of adaptation [65, 73]. We comment on how adaptation is affected by the type of output of Stage 5, using either the approximations from the effective models, the average or instantaneous firing rate estimates of the phenomenological models (zilany2014, bruce2018), or the average rates of the biophysical models (verhulst2015, verhulst2018).

#### a. Adaptation.

To illustrate the effect of auditory adaptation, we obtained AN model responses to a 4000-Hz pure tone of 70 dB SPL, duration of 300 ms, that was gated on and off with a cosine ramp of 2.5 ms. The obtained AN responses are shown in Fig. 8. All responses had a prominent amplitude overshoot just after the tone onset which then decreased to a plateau (e.g., between 300 and 340 ms, grey dashed lines). After the tone offset ( $t = 350$  ms),

the AN responses showed an undershoot with decreased amplitudes that subsequently returned to their resting level. This stereotypical behaviour is related to the AN adaptation process.

The waveforms from effective models using the adaptation loops (dau1997, relanoiborra2019, osses2021) are shown in Fig. 8a, where their amplitudes expressed model units (MU) had values between  $-230.5$  MU and  $1440.2$  MU (dau1997), with a strong onset overshoot and a resting position at 0 MU. For king2019 (Fig. 8b), a mild overshoot was observed, whose maximum amplitude ( $1.52 \cdot 10^{-3}$  a.u.) was higher in absolute value than that for the undershoot ( $-1.08 \cdot 10^{-3}$  a.u.). With an observed steady-state peak-to-peak amplitude of  $0.87 \cdot 10^{-3}$  a.u. king2019 is, at this stage, the model that preserves the most temporal fine structure.

For the phenomenological models (zilany2014 and bruce2018), the simulated waveforms using their two types of AN synapse outputs are shown in Fig. 8c–d, based on a PSTH (dark green or brown curves) and mean-rate synapse output (light green or brown curves). The obtained PSTH and mean rate responses in zilany2014 differ in their steady-state values (lower values for the PSTH estimate), while for bruce2018 the difference is in their onset responses, with almost no onset adaptation in the simulated mean-rate output. For the biophysical models (Fig. 8e), the AN synapse outputs represent mean firing rates where a stronger effect of adaptation was observed for verhulst2018 (sky blue), with a plateau after onset that was reached after about 150 ms (at  $t \approx 200$  ms) while for verhulst2015 (red) the plateau is reached shortly after the tone onset.

#### b. Rate-level functions.

Rate-level functions were simulated for a 4000-Hz pure tone presented at levels between 0 and 100 dB SPL with a duration of 300 ms, gated on and off with 2.5-ms cosine ramps. The obtained results are shown in Figs. 9 and 10 for rate-level curves in the steady-state regime and for onset responses, respectively. For all models, average rates are shown (coloured traces) while for the phenomenological and biophysical models (panels c–h), the simulated response for the three types of neurons (HSR, MSR, and LSR) are shown (grey traces).

For the phenomenological and biophysical models, the discharge curves in Fig. 9c–h tend to saturate towards higher levels, which is in line with experimental evidence [e.g., 74].

For the effective models (Fig. 9a,b), with the exception of relanoiborra2019, the simulated rates did not show saturation as a function of level. In relanoiborra2019, the simulated rates were between 70.2 and 83 MU for signal levels beyond 40 dB. This saturation effect results from the combined action of the nonlinear cochlear filter (Stage 3) with the later expansion stage (Stage 5, Fig. 2) that precedes the adaptation loops. Despite the overall lack of saturation in the evaluated effective models when looking at the steady-state outputs, a different situation is observed for the onset responses of Fig. 10, where the responses of the models using adaptation loops had

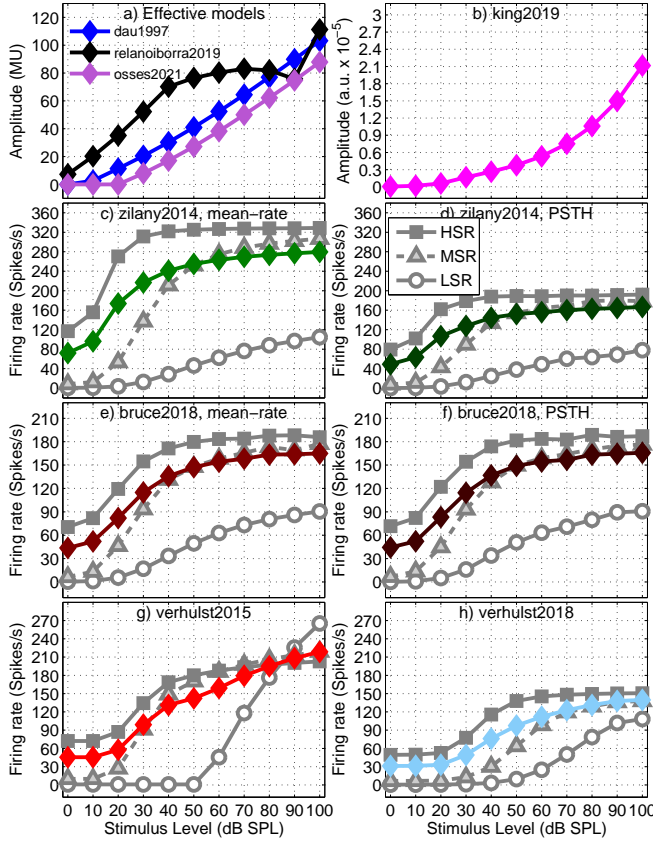


FIG. 9. Simulated rate-level functions derived from the steady-state AN responses of 4000-Hz pure tones. For all models, average responses are shown (coloured traces). For the biophysical and phenomenological models, the responses for HSR, MSR, and LSR neurons are also shown (grey traces). **Literature:** Fig. 7 from [27], Fig. 5A from [26], and Fig. 3 from [35].

a prominent (onset) saturation (dau1997: 1443 MU for levels above 50 dB; relanoiborra2019: 1435 MU for levels above 30 dB; osses2021: 614 MU for levels above 50 dB). Other interesting aspects to highlight are that: (1) almost no onset effect is observed in the mean-rate output of bruce2018; (2) king2019 does not account for any type of saturation as the signal level increases (Figs. 9b, 10b). It should be noted that although hard saturation (as in Fig 10a) has not been experimentally observed for onset AN responses, it is expected a decrease in the growth of onset rate-curves with level [74], a condition that is not met in king2019 nor verhulst2015.

### c. AM model responses.

Model responses were obtained for a 4000-Hz pure tone that was sinusoidally modulated in amplitude (modulation index of 100%) at a rate  $f_{\text{mod}} = 100$  Hz, presented at 60 dB SPL and a duration of 500 ms, including up/down ramps of 2.5 ms. The initial (0-50 ms) and later (350-400 ms) portions of the simulated responses are shown in the left and right panels of Fig. 11, respectively. In all models the modulation rate of 100 Hz is visible as

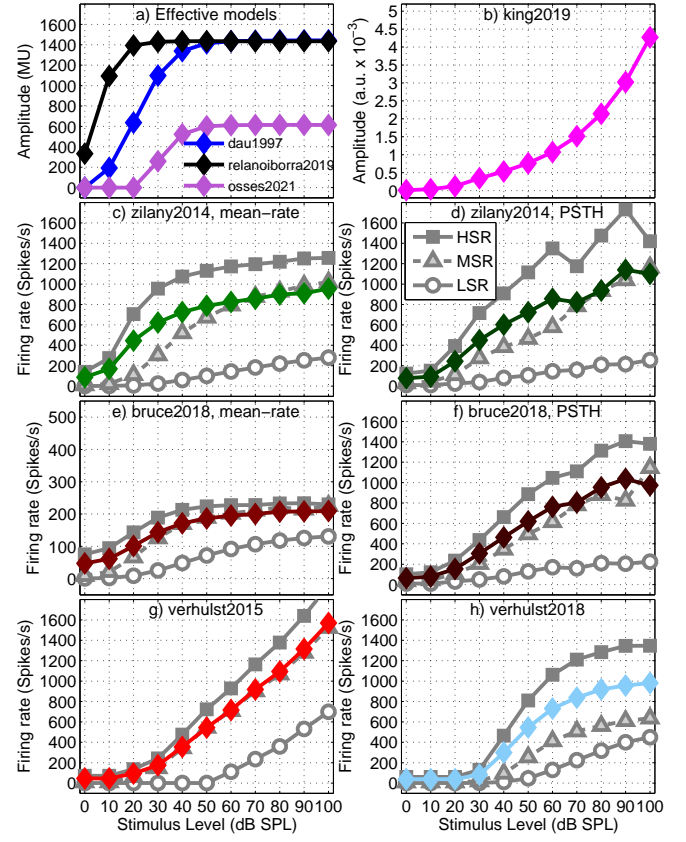


FIG. 10. Simulated rate-level functions derived from the onset (maximum) AN responses of 4000-Hz pure tones. The colour codes and legends are as in Fig. 9. **Literature:** Fig. 3 from [74].

amplitude fluctuations with the corresponding periodicity of 10 ms. In addition, adaptation was observed with stronger simulated responses immediately after the tone onset (left panels) than during the steady-state portion of the response (right panels).

For the effective models with adaptation loops (dau1997, relanoiborra2019, osses2021), the maximum amplitudes (Fig. 11a, left) were much lower in osses2021 than for dau1997 and relanoiborra2019, due to the stronger overshoot limitation. For these models it is also observed that their phases are not perfectly aligned due to the outer and middle ear filters that introduced a delay into relanoiborra2019 (black traces run “ahead” the blue traces of dau1997), while the group-delay compensation in osses2021 (Sec. IIB) seemed to overcompensate the alignment of the simulated waveforms (purple traces run “behind” the blue traces). In the right panel, the dynamic range of relanoiborra2019 (black traces) is lower than for osses2021 and dau1997, which have very similar steady-state amplitudes. The reduced dynamic range in relanoiborra2019 is mainly due to the nonlinear cochlear compression of the filter bank that interacts further with the expansion stage. In king2019 (Fig. 11b), a small effect of adaptation was observed with a maximum onset response of  $0.88 \cdot 10^{-3}$  a.u. (left panel) that decreases to



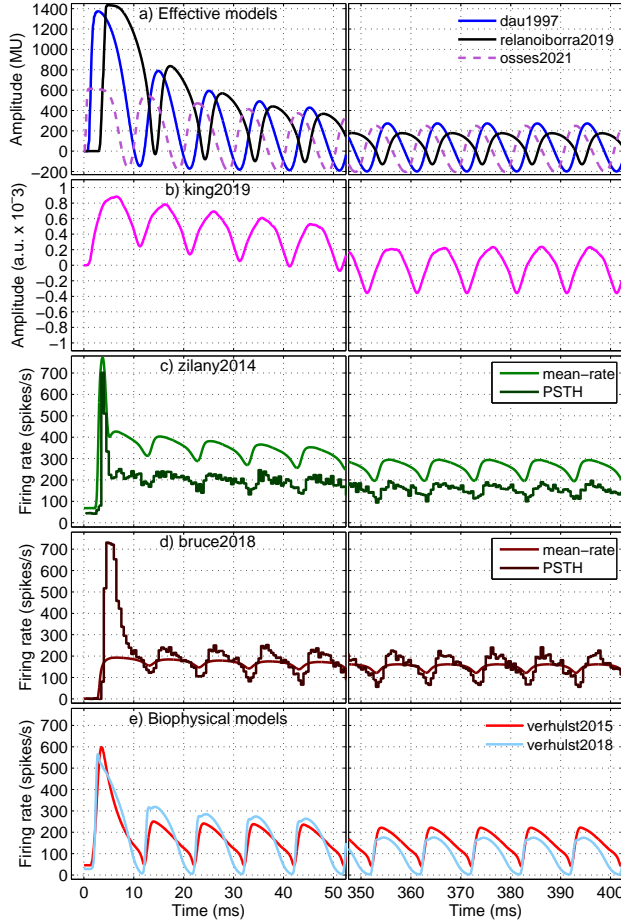


FIG. 11. Simulated on-frequency AN responses to a 4000-Hz tone 100% amplitude-modulated at 100 Hz. **Left:** Onset responses. **Right:** Steady-state responses. **Literature:** Fig. 12 from [65] and Fig. 3C from [26].

a local maximum amplitude of  $0.24 \cdot 10^{-3}$  a.u. during the steady-state response (right panel).

The AN responses produced by *verhulst2015* and *verhulst2018* (panel e) showed an overshoot reaching firing rates of 598.5 and 565.2 spikes/s, respectively. After the onset, the overshoot effect quickly disappeared in *verhulst2015*, reaching a maximum local rate of 251 spikes/s during the second modulation cycle and 222 spikes/s between 370 and 400 ms. In contrast, *verhulst2018* adapted more slowly after the onset with a maximum rate of 319 spikes/s in response to the second modulation cycle, while the response continued adapting reaching a maximum rate of 176 spikes/s between times 370 and 400 ms.

For *zilany2014* (Fig. 11c) and *bruce2018* (Fig. 11d), the mean-rate and PSTH outputs are shown as lighter and darker traces, respectively. It can be observed that in *zilany2014*, the AM modulations showed a similar mean-rate and PSTH excursions of about 100 spikes/s (Fig. 11b, right: mean rates between 194 and 295 spikes/s; PSTHs with rates between 94 and 196 spikes/s), but the PSTHs had overall lower rates. In *bruce2018*, a greater AM fluctuation is observed for

the PSTHs outputs (darker brown traces) with an excursion of 185 spikes/s (Fig. 11d, right: rates between 56 and 241 spikes/s) compared with the 40 spikes/s (rates between 121 and 161 spikes/s) of its mean-rate output. Additionally, *bruce2018* showed a limited effect of adaptation in its mean-rate outputs, also showing a shallower AM response in comparison to the obtained PSTH. We will not focus on the mean-rate output of this model, because (1) their authors validated the model primarily using PSTHs, recommending the use of that AN synapse output for further processing [27], (2) the model using PSTH outputs can be used as input for subcortical processing stages in the UR EAR toolbox [58], and (3) all the studies that we have so far identified using *bruce2018* consistently used PSTHs outputs [75, 76].

It should be noted that the *zilany2014* model, from the same model family, has been extensively validated using both mean-rate and PSTHs outputs. In fact, for studies where psychoacoustic aspects have been investigated [e.g., 57] there is a tendency to use the mean-rate model outputs.

#### d. Synchrony capture.

Model responses were obtained for a complex tone of 50 dB SPL formed by three sinusoids of equal peak amplitude and frequencies of 414 Hz (9.6  $ERB_N$ ), 650 Hz (12.6  $ERB_N$ ), and 1000 Hz (15.6  $ERB_N$ ). This type of complex tone with more carriers and greater range of frequencies are commonly used in studies of profile analysis [e.g., 57] and it is useful to explain an interesting AN property named “synchrony capture” [54, 79]. When synchrony capture occurs, the neural activity in on-frequency channels is driven primarily by one frequency component in the harmonic complex, such that there are minimal fluctuations due to the fundamental-frequency envelope, while off-frequency channels exhibit fluctuating AN patterns at the fundamental frequency. To illustrate whether the evaluated models account for synchrony capture, the model outputs in response to the described complex tone were obtained for frequencies between 415 Hz ( $n=320$ ) and 1007 Hz ( $n=245$ , Eq. 3) for CFs spaced at approximately 1  $ERB$  ( $\Delta n = 12$  or 13), resulting in three on-CF and four off-CF channels. The obtained simulations are shown in Fig. 12 for a 30-ms window (between 220 and 250 ms). For each waveform, a schematic metric of envelope fluctuation was obtained and shown as thick grey lines. Those envelope fluctuations were constructed by connecting consecutive local maxima that had amplitudes above the mean responses (onset excluded) of each simulated channel. Subsequently, the standard deviation of the obtained envelope estimate divided by the amplitude scales for each model is indicated in the insets of each panel (e.g., scale of 800 MU for *dau1997*, *relanoiborra2019*, and *osses2021*) were drawn as maroon circles that are connected with dashed lines along the right vertical axes in Fig. 12, with higher values indicating greater envelope fluctuation variability. The scaling used for this estimate allows for a direct comparison between models. In Fig. 12 it can be observed that for all models, the on-frequency channels had nearly flat envelope



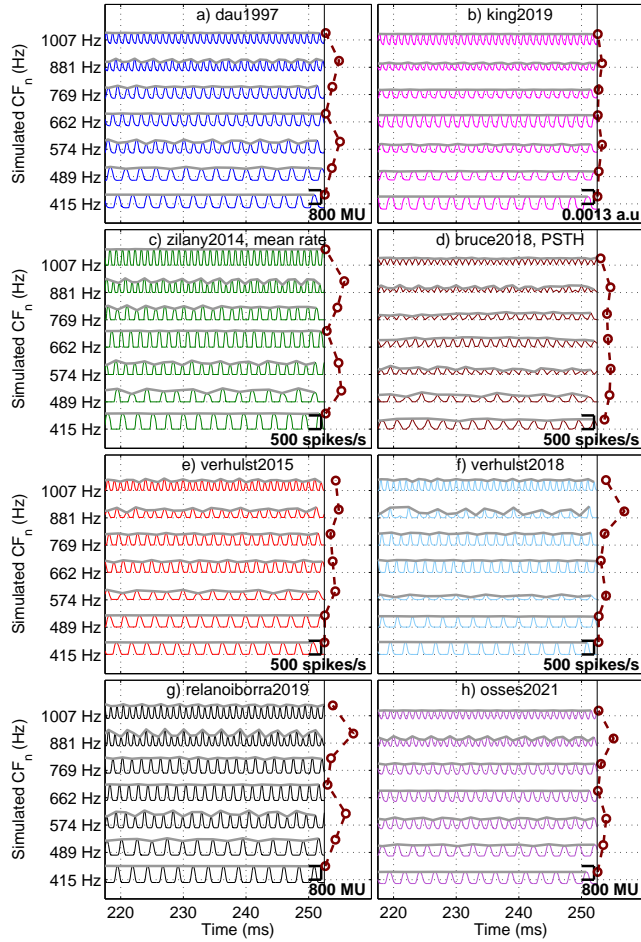


FIG. 12. Simulated AN responses to a complex tone with three frequency components at 414, 650, and 1000 Hz. The model simulations were obtained at on- and off-frequency CFs spaced at 1 ERB. **Literature:** Figs. 7 and 8 from [77] and Fig. 1 from [78].

fluctuations. The variability estimate averaged across on-frequency bins ranged between 0.071 (king2019) and 1.14 (bruce2018). The variability estimate across off-frequency bins ranged between 0.50 (king2019) and 2.72 (relanoiborra2019). For all models the off-CF variability was greater than the on-CF variability, with king2019 being the least sensitive model to code envelope fluctuations.

### E. Subcortical processing

We show two sets of figures to schematise the subcortical processing of the evaluated models.

#### a. Modulation transfer function.

The first set of figures represents a modulation transfer function (MTF) in response to 100% AM tones modulated at  $f_{\text{mod}}$  rates between 10 and 130 Hz (steps of 5 Hz). The tones were centred at 1000 Hz, had a duration of 300 ms, included 5-ms up/down ramps, and were presented at 30 and 70 dB SPL. For this process-

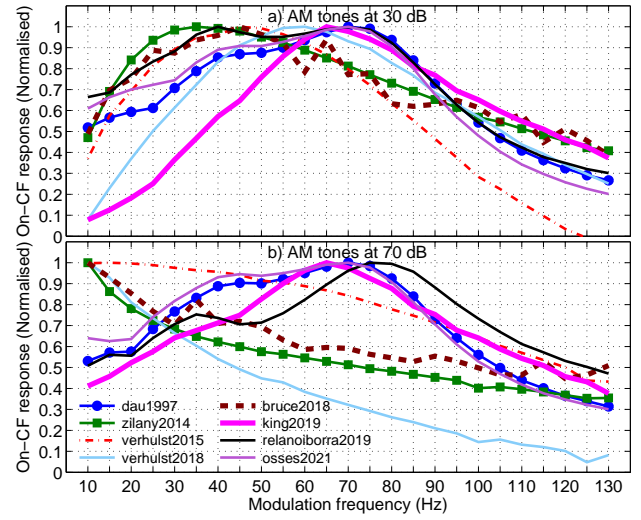


FIG. 13. Modulation transfer functions (MTFs) of a modulation filter with a  $\text{BMF} \approx 80$  Hz, assessed using 1000-Hz AM tones presented at 30 (panel a) or 70 dB SPL (panel b) that were sinusoidally modulated with  $f_{\text{mod}}$  frequencies between 10 and 130 Hz. The MTFs are normalised to the maximum model response across the tested  $f_{\text{mod}}$  frequencies. **Literature:** Figs. 4–6 from [80], Figs. 1 and 4 from [81].

ing, 100 ms in the last portion of the simulated responses were used (between times 190 and 290 ms). The MTFs were assessed from the maximum of the simulated responses. The responses were normalised to the corresponding maximum estimate over the set of tested  $f_{\text{mod}}$  values, so that the MTF of each model had a maximum value of 1. The resulting MTFs are shown in Fig. 13.

The results in Fig. 13a show that the models produce bandpass-shaped MTFs with estimated BMFs between 35 Hz (zilany2014) and 70 Hz (dau1997, relanoiborra2019, and osses2021) that are below the theoretical BMFs (see Table II). It is interesting to observe that the sharpest MTFs were obtained not only for dau1997 and osses2021 (both designed with  $Q=2$ ), but also for king2019 (which has a  $Q=1$ ), while a wider tuning was observed for the remaining models, including relanoiborra2019 (which has a  $Q=2$ ).

For the biophysical and phenomenological models, the MTFs obtained for the 70-dB AM tones (Fig. 13b) were different than those obtained for 30 dB (Fig. 13a). For these models, the MTFs were no longer bell-shaped and seemed to act as lowpass filters, which is inline with physiological evidence indicating that regions of “enhancement” in MTFs of low level-signals can become regions of “suppression” for higher presentation levels (see, e.g., Fig. 4 from [80]).

The effective models were more insensitive to the change in presentation levels. Perhaps the only exception to this is relanoiborra2019, where a narrower MTF was obtained in Fig. 13b (compared with panel a). The models dau1997, osses2021, and king2019 have MTFs that are qualitatively similar across presentation levels.

### b. Response to clicks of alternating polarity.

The second set of figures focuses on simulating the response to a typical click train as used in the assessment of auditory brainstem responses (ABRs) [82]. We used a click train with a repetition rate of 10 Hz and a duration of 1 s (i.e., containing 10 clicks). The clicks had an alternating polarity (amplitude  $A$  or  $-A$ ) and were presented at 70 dB peak-equivalent SPL (dB peSPL) [83], i.e., using  $A = 0.1789$  Pa. Each individual click had a duration of  $100 \mu\text{s}$ . For this processing, the simulated outputs of model Stage 6 (see Fig. 2) were averaged across CFs obtaining a broadband representation, i.e., all simulated representations were added together and were then divided by the number of CFs [25, 26]. This type of output can be used to derive a peak-to-peak or peak-to-trough amplitude correlate of the wave-V ABR component [82].

For this processing, we used the default number of CFs for the biophysical and effective models, while for zilany2014 and bruce2018, 50 CFs were obtained between  $\text{CF}_n = 133.7 \text{ Hz}$  ( $n = 393$ , Eq. 3) and  $\text{CF}_n = 12010 \text{ Hz}$  ( $n = 1$ ), spaced at  $n = 8$  bins to roughly meet the number of filters from Table II. The obtained click responses are shown in Fig. 14.

The biophysical models provided click responses that had positive and negative amplitudes (Fig. 14e–f), which was not the case for the phenomenological models that also use the SFIE model. This is because verhulst2015 and verhulst2018 assume that a population response can be obtained from the sum of single neuron activity (as, e.g., in [48]), with no half-wave rectification in the SFIE model (a non-explicit choice of the authors [25, 26]) that, after scaling [26, 32], results in a simplified neural representation that correlates with changes in electrical dipoles visible in scalp-recorded potentials [26].

The effective models, that use the modulation-filterbank concept, showed only positive amplitudes for all filters with BMFs  $\geq 10 \text{ Hz}$  [22] due to their envelope extraction, a phase-insensitive (“venvelope”) processing [28, 84]. For modulation frequencies below 10 Hz the perceptual models preserve the phase information, something that is not illustrated in Fig. 14 (nor in Fig. 13).

Finally, the simulated peak-to-peak amplitudes in response to the last positive and negative clicks of the pulse train (ninth and tenth click, shown in Fig. 14) are shown in the entries “Click A” and “Click  $-A$ ” of Table II. From those amplitudes it can be observed that there are models that have higher peak-to-peak amplitudes in response to positive clicks (zilany2014, verhulst2015, bruce2018, relanoiborra2019) and others where higher amplitudes are observed in response to the clicks of negative polarity (dau1997, verhulst2018, king2019, osses2021). Although we do not discuss the significance of this polarity sensitivity, this aspect has been a matter of discussion, in particular for electrical hearing, where it has been found that evoked potentials in response to positive and negative polarity clicks represent one of the differences between humans [85, 86] and other mammals [e.g., 87], whose responses are more sensitive to stimulation with clicks of negative and positive polarities, respectively.

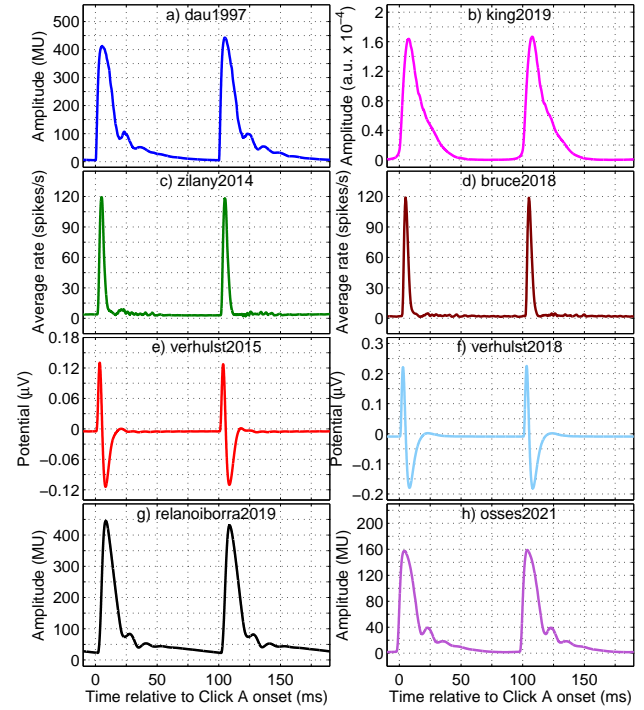


FIG. 14. Simulated IC responses using one modulation filter (BMF  $\approx 80 \text{ Hz}$ ) to a click train of alternating polarity with a total duration of 1 s, repetition rate of 10 Hz and click duration of  $100 \mu\text{s}$ . **Literature:** Fig. 1 from [85] and Figs. 8 and 9 from [82].

### F. Computational costs

The computational cost required to run each model was measured using the same click train as described in the previous section. Therefore, it assesses the time required to process an input signal of 1-s duration between the model stages 1 to 6 (Fig. 2). This metric aims at providing a relative notion of the processing times across models. Note that some model implementations can use parallel processing, which was disabled in this evaluation. The assessment was performed on a personal computer equipped with an Intel Core i5-10210UR, 1.6-GHz processor with 16 GB of RAM memory.

The results of the computational costs used by each model are given in the entry “Performance” of Table II. The time required by the models to process one frequency channel ranged between  $\sim 0.02 \text{ s}$  (osses2021, dau1997) and  $2.5 \text{ s}$  (bruce2018). For individual frequency channels, the biophysical models (verhulst2015 and verhulst2018) showed moderate calculation times between 0.3 and 0.8 s, however, these models always require (internally) the simulation of the whole discretised cochlea with 1000 cochlear sections, independent of the number of user-requested cochlear channels (default number of 401 for the Verhulst models). This means for the current simulations, that the reported processing times of 122.9 and 319.5 s for verhulst2015 and verhulst2018, respectively, cannot be further reduced, even if the user requests the

simulation of less CFs. In contrast, in any model based on a parallel filter bank, including *zilany2014* and *bruce2018*, each cochlear section is independent of each other, and a user-defined number of frequency channels can be simulated, which vastly reduces the computation time for different model configurations.

Due to the long processing time of the evaluated biophysical models, their implementations include an option of parallel processing (also available in the original implementation of *bruce2018* [27]), where multiple input signals can be processed simultaneously. The number of signals that can be processed in parallel will depend on the number of threads of the host computer. As a further solution to the long processing time, the transmission-line, IHC, and AN modules of *verhulst2018* have been approximated using a convolutional neural-network approach [88, 89].

## V. MODELS IN PERSPECTIVE

The stimuli and comparison measures used in our evaluation (Sec. IV) were chosen to reflect relevant temporal and spectral properties of the models in a normal-hearing condition. Our evaluation was meant to provide an objective view accompanied by a graphical representation of how the model responses could account for specific aspects of the hearing processing according to their model structure. In the current section we provide a brief overview of the context in which each of the selected models has been used, including some general recommendations for further applications.

### A. Applicability of the models for monaural processing

*Dau1997* is a monaural model that has been used to simulate a number of psychoacoustic tasks including tone-in-noise and AM detection experiments using a forced-choice paradigm [e.g., 22, 35]. To enable the model for the comparison between two or more sounds, the output of Stage 6 (Fig. 2) is used as input to a decision back-end based on a signal-detection-theory (SDT) framework: the template-matching approach. This framework, extended to adopt two templates, has been recently validated to account for the perceptual similarity between two sounds using *osses2021* [30].

The models *zilany2014* and *bruce2018* can account for elevated hearing thresholds due to OHC (“Cochlear gain loss” in Stage 3) or IHC impairment (“IHC loss” in Stage 4) [47]. The AN stage (Stage 5) includes two types of outputs: an actual spike generator and an analytical mean-rate synapse output. The spike generator has been primarily used to simulate physiological data, including the phenomenon of short- and long-term adaptation [65]. The mean-rate synapse output using *zilany2014* has been used to simulate specific psychoacoustic tasks [57, 90].

The models *verhulst2015* and *verhulst2018* were initially designed to simulate otoacoustic emissions [46] and can account for elevated hearing thresholds due to OHC impairment (“Cochlear gain loss” in Stage 3). Further-

more, they allow to study effects of the gradual disconnection of AN fibres, known as synaptopathy, on auditory brainstem responses [26, 91]. When coupled with a decision back-end, they can simulate psychoacoustic performance in simultaneous tone-in-noise and high-rate AM tasks ( $f_{\text{mod}} \sim 100\text{--}120$  Hz) [92, 93].

The model *relanoiborra2019* can predict speech intelligibility [29] when coupled with a decision back-end stage [29, 94]. Relying on the prediction power of earlier model implementations, *relanoiborra2019* should be able to (1) account for elevated thresholds based on OHC and IHC impairment [95], and (2) to predict a number of psychoacoustic tasks including simultaneous and forward masking and amplitude modulation [96]. Our results showed that *relanoiborra2019* accounts well for hearing properties such as nonlinearities in the cochlear processing and auditory adaptation, including a saturation behaviour similar to that of the AN physiological models.

The model *king2019* was designed to simulate perceptual tasks of amplitude and frequency modulation detection, primarily at low modulation rates ( $f_{\text{mod}} \leq 20$  Hz), including deterministic limitations (suboptimal template matching strategies) or stochastic limitations such as internal additive noise, multiplicative noise [97], and memory noise [98]. The model can be adapted to simulate hearing impairment by modifying its compression parameters (knee point and compression rate), and increasing the width of the underlying cochlear filters. Despite the simplicity of this model—in fact one of its strengths—we have shown in this paper that the model can account for several of the comparison metrics, with the exception of the narrowing of cochlear filters at higher presentation levels (Fig. 5) and the adaptation saturation (Figs. 9–10).

### B. Applicability of the models for binaural processing

Models of binaural processing rely on simulating the monaural processing up to the AN level [2]. For this reason it is not surprising that several of the tested models have been used as preprocessing stages for binaural back-ends. The lowpass modulation filter (similar to *dau1997*) [22, 35] served as the basis for a model of binaural masking that uses a decision stage based on the equalisation-cancellation theory [99]. This model was later extended to predict perceptual attributes of room acoustics [100, 101]. The model *zilany2014* has been used to predict the sensitivity to interaural time and level differences by estimating the disparity between left and right AN responses using a decision back-end based on shuffled cross-correlograms [102]. Finally, *bruce2018* has been used to simulate the lateralisation of high-frequency stimuli in a coincidence-counting model [75].

### C. Simplified auditory representations

In order to broaden our understanding of the auditory processes, computational models that are as complete as possible are required. The more detailed knowledge comes at the price of more computationally-



expensive implementations. Thus, the development of models follows their objective: Biophysical and phenomenological models attempt to shed light on the mechanisms behind the auditory processing and for that purpose they need to be as complete as possible. On the other hand, effective models have a more epistemic status providing an intelligible (simplified) representation of the process and can guide the design of new experiments or the development of listener-targeted products. Such model simplification, however, potentially reduces the number of effects a model can account for, leading to an actual narrowing of its application field. An example of a successful model simplification is presented in [55], where MTFs were simulated using only a stage of envelope extraction followed by a modulation filter bank omitting, thus, the stages of cochlear filtering and auditory adaptation. This model, however, is not thought to predict the performance in listening conditions where the omitted model stages do play a role, as it is the case, in this example, for forward masking tasks.

Peripheral auditory models are often combined with a decision back-end module converting simulated responses into a behavioural response such as detectability or discriminability [e.g., 2] or to obtain perceptual metrics [e.g., 19, 100]. For successful simulations, the decision stage should appropriately weight the information contained in the model representations. An analysis of weighted time-frequency representations (time, audio frequency, and/or modulation frequency) can reveal what portions of the simulated responses are more relevant [e.g., 30, 103].

It is important to note that the simplification of auditory models based on statistical methods or machine learning processes requires a careful interpretation. While these approaches might be well suited to achieve goals as real-time processing [e.g., 88] in applications such as speech perception [e.g., 104] or in the prediction of evoked potentials [76], they limit the modular comprehension of each auditory stage, especially if multiple model stages are approximated [76, 104].

In a recent study [76], firing rates of cortical A1 neurons in ferrets were approximated using several time-frequency representations ranging from simple short-time Fourier transforms to more detailed models of AN synapses (including bruce2018) to which a linear-nonlinear (LNL) encoder was used. Based on their separately-fitted encoders, the authors concluded that cortical processing in ferrets perform a “very simple signal transformation,” without even discussing how different the linear and nonlinear components in each of their encoders were. For this reason, despite the success of the authors in approximating neural responses in ferrets, we believe that it is difficult to know whether the “simple transformation” is indeed related to the underlying system (the cortical processing in ferrets) and not related to the complexity of operations in the fitted encoders.

## D. Considerations for further modelling work

The following is a list of aspects that we recommend to keep in mind for further auditory modelling work, based on the general observations of this study:

- We recommend to use an outer-ear module if the evaluated sounds are assumed to be reproduced via loudspeakers, or supra-aural or circumaural headphones.
- The results in Figs. 5 and 13 show nonlinear interactions between model stages as a function of level and for different types of signals. This suggests that different sets of stimuli are required to characterise the behaviour of complex processes such as that of nonlinear filter banks. In other words, models may not always act as a linear time invariant (LTI) system.
- In Sec. IV B we suggested a minimum number of filters for each filter bank to roughly meet a  $-3$ -dB filter crossing (Table II, “40 dB: Number of bands”). The actual number of bands that are needed may vary from application to application and depend on the type of sounds that are to be simulated. This choice can be particularly critical in models where the number of bands are a free parameter (here zilany2014 and bruce2018). For models that are used as front-ends to machine-learning applications, Lyon [18] suggested a “not-too-sparse set of channels” with about a 50% overlap between filters, i.e., twice the number of channels that we recommend in Table II. It is important to keep in mind, however, that our estimation was based on model responses to white noises, which are sustained signals in time and broadband in frequency. At higher presentation levels, where nonlinear filter banks are compressive, similar estimations using sine tones (sustained narrowband signals, as in Fig. 4) or clicks (transient broadband sounds) may result in a different number of required bands.
- Different simulation results can be expected when evaluating mean-rate and PSTH outputs of models including AN synapse stages as shown in Figs. 8–11. The particular choice of the type of output depends on the target application of the model. The spike generator is primarily used to simulate physiological data [e.g., 27, 65], while the mean-rate synapse output is typically used to simulate specific psychoacoustic tasks [e.g., 57, 90].

## VI. CONCLUSIONS

In this paper we compared eight models of auditory processing that simulate responses –with different levels of accuracy– up to the level of the inferior colliculus in the midbrain. We described and quantified the similarities and differences among model implementations, and we derived a minimum number of filters required for those stages to ensure the preservation of auditory information based on our estimates of frequency selectivity.

We showed that despite the differences in model design that result in more physiologically- (biophysical and



phenomenological models) or perceptually-plausible approximations (effective models), the models can still account for a considerable number of hearing properties. Examples of these properties are the phase-locking reduction in inner-hair-cell processing and the phenomenon of auditory adaptation. Still, an in-depth understanding of each of the model stages is required when selecting a model for an application and to compare the models to one another. We encourage future users to be explicitly aware of the specific datasets of sounds and experimental paradigms upon which their models have been evaluated and the underlying model limitations. The further use of back-end modules, e.g., based on machine learning, statistics, or signal detection theory, may help to better facilitate the information obtained from auditory models. To this end, the comparison across model implementations provides a guideline for their selection and excellent way to challenge the capabilities of the different models.

## ACKNOWLEDGEMENTS

We are grateful to several colleagues who participated in technical discussions during the writing process: Enrique Lopez-Poveda, Fotios Drakopoulos, Alessandro Altoè, Armin Kohlrausch, and Richard Lyon. We are particularly grateful to Clara Hollomey, who provided immense support for the integration of all models into AMT 1.0. The authors AOV and LV. received support from ANR (project: 17-EURE-0017), SV received support from the ERC project RobSpear (Grant No. 678120), and PM received support from the H2020 project SONICOM (EC Grant No. 101017743).

## Footnotes

<sup>1</sup>In this study we adopted the spelling “neuron” instead of “neurone,” following the etymological argument from [105].

## References

- [1] R. Meddis, E. Lopez-Poveda, R. Fay, and A. Popper, eds., *Computational Models of the Auditory System*, Springer Handbook of Auditory Research (Springer, 2010).
- [2] T. Dau, “Auditory Processing Models,” in *Handbook of Signal Processing in Acoustics*, edited by D. Havelock, S. Kuwano, and M. Vorländer (Springer, 2008), pp. 175–196, doi: [10.1007/978-0-387-30441-0\\_12](https://doi.org/10.1007/978-0-387-30441-0_12).
- [3] M. Dietz, S. Ewert, and V. Hohmann, “Auditory model based direction estimation of concurrent speakers from binaural signals,” *Speech Communication* **53**, 592–605 (2011) doi: [10.1016/j.specom.2010.05.006](https://doi.org/10.1016/j.specom.2010.05.006).
- [4] G. Bustamante, P. Danès, T. Fergie, A. Podlubne, and J. Manhès, “An information based feedback control for audio-motor binaural localization,” *Auton. Robot.* **42**, 477–490 (2018) doi: [10.1007/s10514-017-9639-8](https://doi.org/10.1007/s10514-017-9639-8).
- [5] R. Peng, “Reproducible research in computational science,” *Science* **334**(6060), 1226–1227 (2011) doi: [10.1126/science.1213847](https://doi.org/10.1126/science.1213847).
- [6] R. Patterson, M. Allerhand, and C. Giguère, “Time-domain modeling of peripheral auditory processing: a modular architecture and a software platform,” *J. Acoust. Soc. Am.* **98**, 1890–1894 (1995) doi: [10.1121/1.414456](https://doi.org/10.1121/1.414456).
- [7] B. Fontaine, D. Goodman, V. Benichoux, and R. Brette, “Brian hears: Online auditory processing using vectorization over channels,” *Front. Neuroinform.* **5** (2011) doi: [10.3389/fninf.2011.00009](https://doi.org/10.3389/fninf.2011.00009).
- [8] P. Majdak, C. Hollomey, and R. Baumgartner, “AMT 1.0: the toolbox for reproducible research in auditory modeling,” *Acta Acustica* (2021).
- [9] A. Saremi, R. Beutelmann, M. Dietz, G. Ashida, J. Kretzberg, and S. Verhulst, “A comparative study of seven human cochlear filter models,” *J. Acoust. Soc. Am.* **140**, 1618–1634 (2016) doi: [10.1121/1.4960486](https://doi.org/10.1121/1.4960486).
- [10] E. Lopez-Poveda, “Spectral processing by the peripheral auditory system: Facts and models,” *Int. Rev. Neurobiol.* **70**, 7–48 (2005) doi: [10.1016/S0074-7742\(05\)70001-5](https://doi.org/10.1016/S0074-7742(05)70001-5).
- [11] T. Anderson, “A comparison of auditory models for speaker independent phoneme recognition,” in *IEEE Int. Conf. Acoust. Speech Signal Process.* (1993), Vol. 2, pp. 231–234, doi: [10.1109/ICASSP.1993.319277](https://doi.org/10.1109/ICASSP.1993.319277).
- [12] J. Breebaart, S. van de Par, and A. Kohlrausch, “On the difference between cross-correlation and EC-based binaural models,” in *Forum Acusticum*, Sevilla, Spain (2002), pp. 1–6.
- [13] K. Steinmetzger, J. Zaar, H. Relaño-Iborra, S. Rosen, and T. Dau, “Predicting the effects of periodicity on the intelligibility of masked speech: an evaluation of different modelling approaches,” *J. Acoust. Soc. Am.* **146**, 2562–2576 (2019) doi: [10.1121/1.5129050](https://doi.org/10.1121/1.5129050).
- [14] M. Rudnicki, O. Schoppe, M. Isik, F. Völk, and W. Hemmert, “Modeling auditory coding: from sound to spikes,” *Cell and Tissue Research* **361**, 159–175 (2015) doi: [10.1007/s00441-015-2202-z](https://doi.org/10.1007/s00441-015-2202-z).
- [15] M. Dietz, J.-H. Lestang, P. Majdak, R. Stern, T. Marquardt, S. Ewert, W. Hartmann, and D. Goodman, “A framework for testing and comparing binaural models,” *Hear. Res.* **360**, 92–106 (2018) doi: [10.1016/j.heares.2017.11.010](https://doi.org/10.1016/j.heares.2017.11.010).
- [16] P. Søndergaard and P. Majdak, “The Auditory Modeling Toolbox,” in *The Technology of Binaural Listening*, edited by J. Blauert (Springer Berlin Heidelberg, 2013), Chap. 2, pp. 33–56.
- [17] K. Kanders, T. Lorimer, F. Gomez, and R. Stoop, “Frequency sensitivity in mammalian hearing from a fundamental nonlinear physics model of the inner ear,” *Sci. Rep.* **7**, 9931 (2017) doi: [10.1038/s41598-017-09854-2](https://doi.org/10.1038/s41598-017-09854-2).
- [18] R. Lyon, “Cascades of two-pole-two-zero asymmetric resonators are good models of peripheral auditory function,” *J. Acoust. Soc. Am.* **130**, 3893–3904 (2011) doi: [10.1121/1.3658470](https://doi.org/10.1121/1.3658470).
- [19] B. Moore, B. Glasberg, and T. Baer, “A model for the prediction of thresholds, loudness and partial loudness,” *J. Audio Eng. Soc.* **45**, 224–240 (1997).
- [20] A. Osses Vecchi, R. García León, and A. Kohlrausch, “Modelling the sensation of fluctuation strength,” *Proc. Mtgs. Acoust.* **28**(050005), 1–8 (2016) doi: [10.1121/2.0000410](https://doi.org/10.1121/2.0000410).
- [21] B. Laback, M. Dietz, and P. Joris, “Temporal effects in interaural and sequential level difference perception,” *J. Acoust. Soc. Am.* **142**, 3267–3283 (2017) doi: [10.1121/1.5009563](https://doi.org/10.1121/1.5009563).
- [22] T. Dau, B. Kollmeier, and A. Kohlrausch, “Modeling auditory processing of amplitude modulation. I. Detection and masking with narrow-band carriers,” *J. Acoust. Soc. Am.* **102**, 2892–2905 (1997) doi: [10.1121/1.420344](https://doi.org/10.1121/1.420344).
- [23] M. Zilany, I. Bruce, and L. Carney, “Updated parameters and expanded simulation options for a model of the auditory periphery,” *J. Acoust. Soc. Am.* **135**, 283–286 (2014) doi: [10.3389/fphar.2018.00665](https://doi.org/10.3389/fphar.2018.00665).
- [24] L. Carney, T. Li, and J. McDonough, “Speech coding in the brain: Representation of vowel formants by midbrain neurons tuned to sound fluctuations,” *eNeuro* **2**, 1–12 (2015) doi: [10.1523/ENEURO.0004-15.2015](https://doi.org/10.1523/ENEURO.0004-15.2015).
- [25] S. Verhulst, H. Bharadwaj, G. Mehraei, C. Shera, and B. Shinn-Cunningham, “Functional modeling of the human auditory brainstem response to broadband stimulation,” *J. Acoust. Soc. Am.* **138**, 1637–1659 (2015) doi: [10.1121/1.420344](https://doi.org/10.1121/1.420344).

TABLE II. Model configurations and numeric results. **Middle ear:** Details of frequency response of the middle-ear filters. **Cochlear filter bank:** 40 dB and 100 dB refer to filter characteristics between 160 and 8000 Hz in response to white noises of 40 and 100 dB SPL, respectively. **IHC:** Parameters and frequency response of the LP filter structures. **Subcortical processing:** Theoretical and estimated BMF of the modulation filter with the closest BMF to 100 Hz and peak-to-peak amplitude of the simulated IC outputs in response to 70-dB-peSPL clicks of positive ( $A$ ) and negative ( $-A$ ) (see Sec. IV E for more details). **Performance:** Time required to process a 1-s long stimulus using each of the selected auditory models, between Stages 1 and 6 (Fig. 2). All  $f_{\text{cut-off}}$  in this table were measured at the  $-3$  dB points of the amplitude spectrum.

Stage Parameter	Model							
	dau1997	zilany2014	verhulst2015	verhulst2018	bruce2018	king2019	relanoiborra2019	osses2021
<b>Middle ear</b>								
Passband gain in Fig. 3 (dB)	–	–6.0	24.0	18.0	–6.0	–	–66.9	0.00
Lower $f_{\text{cut-off}}$ (Hz)	–	577.6	601.0	601.1	577.6	–	474.8	474.8
Higher $f_{\text{cut-off}}$ (Hz)	–	6061.9	2995.3	3993.1	6061.9	–	1230.2	1230.2
<b>Cochlear filter bank</b>								
Reference gain in Fig. 4 (dB)	–0.6	–44.1	–77.9	–101.9	–44.1	–43.9	26.9	–1.9
40 dB: Number of filters	34	51	59	52	51	34	36	34
40 dB: Average filter bandwidth (ERB)	0.903	0.588	0.505	0.579	0.588	0.904	0.848	0.905
100 dB: Number of filters	34	20	12	15	20	33	27	34
100 dB: Average filter bandwidth (ERB)	0.903	1.57	3.046	2.299	1.57	0.925	1.147	0.905
<b>IHC</b>								
Number of filter sections	1	7	1	–	7	1	1	5
Order of each filter section	1	1	2	–	1	1	2	1
$f_{\text{cut-off}}$ of each filter section (Hz)	1000	3000	1000	–	3000	1000	1000	2000
$f_{\text{cut-off}}$ of the total filter structure (Hz)	1000	966	642	–	966	1000	1000	771
<b>Subcortical processing</b>								
Theoretical BMF (Hz)	77.2	85.4	82.4	82.4	85.4	94.0	77.2	77.2
Estimated BMF from Fig. 13a (Hz)	70	35	45	60	45	65	70	70
Unit of the amplitude	MU	spikes/s	$\mu\text{V}$	$\mu\text{V}$	spikes/s	a.u.	MU	MU
Click of amplitude $A$	407.3	116.5	0.245	0.401	117.6	$1.64 \cdot 10^{-4}$	423.1	155.9
Click of amplitude $-A$	437.4	115.8	0.237	0.407	117.3	$1.67 \cdot 10^{-4}$	408.9	157.3
<b>Performance</b>								
Total time (s)	0.80	86.6	122.9	319.5	163.1	1.86	7.70	0.622
Number of cochlear channels	31	66	401	401	66	31	60	31
Time per channel (s)	0.026	1.31	0.306	0.797	2.47	0.060	0.128	0.020

10.1121/1.4928305.

- [26] S. Verhulst, A. Altoè, and V. Vasilkov, “Computational modeling of the human auditory periphery: Auditory-nerve responses, evoked potentials and hearing loss,” *Hear. Res.* **360**, 55–75 (2018) doi: [10.1016/j.heares.2017.12.018](https://doi.org/10.1016/j.heares.2017.12.018).
- [27] I. Bruce, Y. Erfani, and M. Zilany, “A phenomenological model of the synapse between the inner hair cell and auditory nerve: Implications of limited neurotransmitter release sites,” *Hear. Res.* **360**, 40–54 (2018) doi: [10.1016/j.heares.2017.12.016](https://doi.org/10.1016/j.heares.2017.12.016).
- [28] A. King, L. Varnet, and C. Lorenzi, “Accounting for masking of frequency modulation by amplitude modulation with the modulation filter-bank concept,” *J. Acoust. Soc. Am.* **145**, 2277–2293 (2019) doi: [10.1121/1.5094344](https://doi.org/10.1121/1.5094344).
- [29] H. Relano-Iborra, J. Zaar, and T. Dau, “A speech-based computational auditory signal processing and perception model,” *J. Acoust. Soc. Am.* **146**, 3306–3317 (2019) doi: [10.1121/1.5129114](https://doi.org/10.1121/1.5129114).
- [30] A. Osses Vecchi and A. Kohlrausch, “Perceptual similarity between piano notes: Simulations with a template-based perception model,” *J. Acoust. Soc. Am.* 3534–3352 (2021) doi: [10.1121/10.0004818](https://doi.org/10.1121/10.0004818).
- [31] A. Gelfert, “Strategies and Trade-Offs in Model-Building,” in *How to Do Science with Models: A Philosophical Primer* (Springer International Publishing, 2016), pp. 43–70, doi: [10.1007/978-3-319-27954-1\\_3](https://doi.org/10.1007/978-3-319-27954-1_3).
- [32] A. Osses Vecchi and S. Verhulst, “Release note on version 1.2 of the Verhulst et al. 2018 model of the human auditory system: Calibration and reference simulations,” *ArXiv* (2019) [arXiv:1912.10026](https://arxiv.org/abs/1912.10026).
- [33] S. Verhulst, A. Altoè, V. Vasilkov, and A. Osses, “Verhulst et al 2018 Auditory Model v1.2” (2020), <https://github.com/HearingTechnology/Verhulstetal2018Model/releases> doi: [10.5281/zenodo.3717800](https://doi.org/10.5281/zenodo.3717800).
- [34] P. Nelson and L. Carney, “A phenomenological model of peripheral and central neural responses to amplitude-modulated tones,” *J. Acoust. Soc. Am.* **116**, 2173–2186 (2004) doi: [10.1121/1.1784442](https://doi.org/10.1121/1.1784442).
- [35] T. Dau, D. Püschel, and A. Kohlrausch, “A quantitative model of the effective signal processing in the auditory system. I. Model structure,” *J. Acoust. Soc. Am.* **99**, 3615–3622 (1996) doi: [10.1121/1.414959](https://doi.org/10.1121/1.414959).

- [36] J. Rosowski, "The effects of external- and middle-ear filtering on auditory threshold and noise-induced hearing loss," *J. Acoust. Soc. Am.* **90**, 124–135 (1991) doi: [10.1121/1.401306](https://doi.org/10.1121/1.401306).
- [37] H. Møller, M. Sørensen, D. Hammershøi, and C. Jensen, "Head-related transfer functions of human subjects," *J. Audio Eng. Soc.* **43**, 300–321 (1995).
- [38] S. Puria, "Measurements of human middle ear forward and reverse acoustics: Implications for otoacoustic emissions," *J. Acoust. Soc. Am.* **113**, 2773–2789 (2003) doi: [10.1121/1.1564018](https://doi.org/10.1121/1.1564018).
- [39] R. Ibrahim and I. Bruce, "Effects of peripheral tuning on the auditory nerve's representation of speech envelope and temporal fine structure cues," in *The Neurophysiological Bases of Auditory Perception*, edited by R. Meddis, A. Palmer, and E. Lopez-Poveda, pp. 429–438, doi: [10.1007/978-1-4419-5686-6](https://doi.org/10.1007/978-1-4419-5686-6).
- [40] R. Ibrahim, "The role of temporal fine structure cues in speech perception," Ph.D. thesis, McMaster University, 2012, <http://hdl.handle.net/11375/11980>.
- [41] S. Puria, W. Peake, and J. Rosowski, "Sound-pressure measurements in the cochlear vestibule of human-cadaver ears," *J. Acoust. Soc. Am.* **101**, 2754–2770 (1997) doi: [10.1121/1.418563](https://doi.org/10.1121/1.418563).
- [42] E. Lopez-Poveda and R. Meddis, "A human nonlinear cochlear filterbank," *J. Acoust. Soc. Am.* **110**, 3107–3118 (2001) doi: [10.1121/1.1416197](https://doi.org/10.1121/1.1416197).
- [43] R. Goode, M. Killion, K. Nakamura, and S. Nishihara, "New knowledge about the function of the human middle ear: Development of an improved analog model," *Am. J. Otol.* **15**, 145–154 (1994).
- [44] C. Shera, J. Guinan, and A. Oxenham, "Revised estimates of human cochlear tuning from otoacoustic and behavioral measurements," *Proc. Natl. Acad. Sci.* **99**, 3318–3323 (2002) doi: [10.1073/pnas.032675099](https://doi.org/10.1073/pnas.032675099).
- [45] B. Glasberg and B. Moore, "Derivation of auditory filter shapes from notched-noise data," *Hear. Res.* **47**, 103–138 (1990) doi: [10.1016/0378-5955\(90\)90170-T](https://doi.org/10.1016/0378-5955(90)90170-T).
- [46] S. Verhulst, T. Dau, and C. Shera, "Nonlinear time-domain cochlear model for transient stimulation and human otoacoustic emission," *J. Acoust. Soc. Am.* **132**, 3842–8 (2012) doi: [10.1121/1.4763989](https://doi.org/10.1121/1.4763989).
- [47] M. Zilany and I. Bruce, "Modeling auditory-nerve responses for high sound pressure levels in the normal and impaired auditory periphery," *J. Acoust. Soc. Am.* **120**, 1446–1466 (2006) doi: [10.1121/1.2225512](https://doi.org/10.1121/1.2225512).
- [48] F. Rønne, T. Dau, J. Harte, and C. Elberling, "Modeling auditory evoked brainstem responses to transient stimuli," *J. Acoust. Soc. Am.* **131**, 3903–3913 (2012) doi: [10.1121/1.3699171](https://doi.org/10.1121/1.3699171).
- [49] V. Hohmann, "Frequency analysis and synthesis using a Gammatone filterbank," *Acust. Acta Acust.* **88**, 433–442 (2002).
- [50] L. Westerman and R. Smith, "A diffusion model of the transient response of the cochlear inner hair cell synapse," *J. Acoust. Soc. Am.* **83**, 2266–2276 (1988) doi: [10.1121/1.396357](https://doi.org/10.1121/1.396357).
- [51] A. Altoè, V. Pulkki, and S. Verhulst, "Model-based estimation of the frequency tuning of the inner-hair-cell stereocilia from neural tuning curves," *J. Acoust. Soc. Am.* **141**, 4438–4451 (2017) doi: [10.1121/1.4985193](https://doi.org/10.1121/1.4985193).
- [52] A. Peterson and P. Heil, "A simple model of the inner-hair-cell ribbon synapse accounts for mammalian auditory-nerve-fiber spontaneous spike times," *Hear. Res.* **363**, 1–27 (2018) doi: [10.1016/j.heares.2017.09.005](https://doi.org/10.1016/j.heares.2017.09.005).
- [53] P. Majdak, R. Baumgartner, and C. Jenny, "Formation of Three-Dimensional Auditory Space," in *The Technology of Binaural Understanding* (Springer International Publishing, 2020), pp. 115–149, doi: [10.1007/978-3-030-00386-9\\_5](https://doi.org/10.1007/978-3-030-00386-9_5).
- [54] L. Carney, "Supra-threshold hearing and fluctuation profiles: Implications for sensorineural and hidden hearing loss," *J. Assoc. Res. Otolaryngol.* **19**, 331–352 (2018) doi: [10.1007/s10162-018-0669-5](https://doi.org/10.1007/s10162-018-0669-5).
- [55] S. Ewert and T. Dau, "Characterizing frequency selectivity for envelope fluctuations," *J. Acoust. Soc. Am.* **108**, 1181–1196 (2000) doi: [10.1121/1.1288665](https://doi.org/10.1121/1.1288665).
- [56] G. Ashida, D. Tollin, and J. Kretzberg, "Physiological models of the lateral superior olive," *PLoS Computational Biology* **13**, 1–50 (2017) doi: [10.1371/journal.pcbi.1005903](https://doi.org/10.1371/journal.pcbi.1005903).
- [57] B. Maxwell, V. Richards, and L. Carney, "Neural fluctuation cues for simultaneous notched-noise masking and profile-analysis tasks: Insights from model midbrain responses," *J. Acoust. Soc. Am.* **147**, 3523–3537 (2020) doi: [10.1121/10.0001226](https://doi.org/10.1121/10.0001226).
- [58] L. Carney, "University of Rochester: Envisioning Auditory Responses (UR EAR 2020b)" (2020), <https://osf.io/6bsnt/>.
- [59] W. Gerstner, W. Kistler, R. Naud, and L. Paninski, "Variability of spike trains and neural codes," in *Neuronal Dynamics: From Single Neurons to Networks and Models of Cognition* (Cambridge University Press, 2014), Chap. 7, doi: [10.1017/CB09781107447615](https://doi.org/10.1017/CB09781107447615).
- [60] A. Kohlrausch, R. Fassel, and T. Dau, "The influence of carrier level and frequency on modulation and beat-detection thresholds for sinusoidal carriers," *J. Acoust. Soc. Am.* **108**, 723–734 (2000) doi: [10.1121/1.429605](https://doi.org/10.1121/1.429605).
- [61] J. Verhey, T. Dau, and B. Kollmeier, "Within-channel cues in comodulation masking release (CMR): experiments and model predictions using a modulation-filterbank model," *J. Acoust. Soc. Am.* **106**, 2733–2745 (1999) doi: [10.1121/1.428101](https://doi.org/10.1121/1.428101).
- [62] D. Greenwood, "A cochlear frequency position function for several species—29 years later," *J. Acoust. Soc. Am.* **87**, 2592–2605 (1990) doi: [10.1121/1.399052](https://doi.org/10.1121/1.399052).
- [63] M. C. Liberman, "Auditory-nerve response from cats raised in a low-noise chamber," *J. Acoust. Soc. Am.* **63**, 442–455 (1978) doi: [10.1121/1.381736](https://doi.org/10.1121/1.381736).
- [64] M. C. Liberman, L. Dodds, and S. Pierce, "Afferent and efferent innervation of the cat cochlea: Quantitative analysis with light and electron microscopy," *J. Comp. Neurol.* **301**, 443–460 (1990) doi: [10.1002/cne.903010309](https://doi.org/10.1002/cne.903010309).
- [65] M. Zilany, I. Bruce, P. Nelson, and L. Carney, "A phenomenological model of the synapse between the inner hair cell and auditory nerve: Long-term adaptation with power-law dynamics," *J. Acoust. Soc. Am.* **126**, 2390–2412 (2009) doi: [10.1121/1.3238250](https://doi.org/10.1121/1.3238250).
- [66] L. Robles and M. Ruggero, "Mechanics of the mammalian cochlea," *Physiol. Rev.* **81**, 1305–1352 (2001) doi: [10.1152/physrev.2001.81.3.1305](https://doi.org/10.1152/physrev.2001.81.3.1305).
- [67] A. Palmer and I. Russell, "Phase-locking in the cochlear nerve of the guinea-pig and its relation to the receptor potential of inner hair-cells," *Hear. Res.* **24**, 1–15 (1986) doi: [10.1016/0378-5955\(86\)90002-X](https://doi.org/10.1016/0378-5955(86)90002-X).
- [68] E. Lopez-Poveda and A. Eustaquio-Martín, "A biophysical model of the inner hair cell: The contribution of potassium currents to peripheral auditory compression," *J. Assoc. Res. Otolaryngol.* **7**, 218–235 (2006) doi: [10.1007/s10162-006-0037-8](https://doi.org/10.1007/s10162-006-0037-8).
- [69] J. Antoni, "Orthogonal-like fractional-octave-band filters," *J. Acoust. Soc. Am.* **127**, 884–895 (2010) doi: [10.1121/1.3273888](https://doi.org/10.1121/1.3273888).
- [70] A. Altoè, V. Pulkki, and S. Verhulst, "Transmission line cochlear models: Improved accuracy and efficiency," *J. Acoust. Soc. Am.* **136**, EL302–EL308 (2014) doi: [10.1121/1.4896416](https://doi.org/10.1121/1.4896416).
- [71] M. Ruggero, N. Rich, A. Recio, S. S. Narayan, and L. Robles, "Basilar-membrane responses to tones at the base of the chinchilla cochlea," *J. Acoust. Soc. Am.* **101**, 2151–2163 (1997) doi: [10.1121/1.418265](https://doi.org/10.1121/1.418265).



- [72] T. Ren, "Longitudinal pattern of basilar membrane vibration in the sensitive cochlea," *Proc. Natl. Acad. Sci.* **99**, 17101–17106 (2002) doi: [10.1073/pnas.262663699](https://doi.org/10.1073/pnas.262663699).
- [73] B. Moore, *An Introduction to the Psychology of Hearing*, sixth ed. (Koninklijke Brill NV, 2013).
- [74] R. Smith and M. Brachman, "Operating range and maximum response of single auditory nerve fibers," *Brain Research* **184**, 499–505 (1980) doi: [10.1016/0006-8993\(80\)90817-3](https://doi.org/10.1016/0006-8993(80)90817-3).
- [75] J. Klug, L. Schmors, G. Ashida, and M. Dietz, "Neural rate difference model can account for lateralization of high-frequency stimuli," *J. Acoust. Soc. Am.* **148**, 678–691 (2020) doi: [10.1121/1.50001602](https://doi.org/10.1121/1.50001602).
- [76] M. Rahman, B. Willmore, A. King, and N. Harper, "Simple transformations capture auditory input to cortex," *Proc. Natl. Acad. Sci.* **117**, 28442–28451 (2020) doi: [10.1073/pnas.1922033117](https://doi.org/10.1073/pnas.1922033117).
- [77] L. Deng and C. D. Geisler, "Responses of auditory-nerve fibers to nasal consonant-vowel syllables," *J. Acoust. Soc. Am.* **82**, 1977–1988 (1987) doi: [10.1121/1.395642](https://doi.org/10.1121/1.395642).
- [78] L. Carney, D. Kim, and S. Kuwada, "Speech Coding in the Midbrain: Effects of Sensorineural Hearing Loss," in *Physiology, Psychoacoustics and Cognition in Normal and Impaired Hearing*, edited by P. van Dijk, D. Baskent, E. Gaudrain, E. de Kleine, A. Wagner, and C. Lanting (Springer International Publishing, 2016), pp. 427–435, doi: [10.1007/978-3-319-25474-6](https://doi.org/10.1007/978-3-319-25474-6).
- [79] I. Bruce, M. Sachs, and E. Young, "An auditory-periphery model of the effects of acoustic trauma on auditory nerve responses," *J. Acoust. Soc. Am.* **113**, 369–388 (2003) doi: [10.1121/1.1519544](https://doi.org/10.1121/1.1519544).
- [80] B. S. Krishna and M. Semple, "Auditory temporal processing: Responses to sinusoidally amplitude-modulated tones in the inferior colliculus," *J. Neurophysiol.* **84**, 255–273 (2000) doi: [10.1152/jn.2000.84.1.255](https://doi.org/10.1152/jn.2000.84.1.255).
- [81] D. Purcell and M. S. John, "Evaluating the modulation transfer function of auditory steady state responses in the 65 Hz to 120 Hz range," *Ear Hear.* **31**, 667–678 (2010) doi: [10.1097/AUD.0b013e3181e0863b](https://doi.org/10.1097/AUD.0b013e3181e0863b).
- [82] T. Picton, "Auditory brainstem responses: peaks along the way," in *Human Auditory Evoked Potentials* (Plural Publishing, 2011), Chap. 8, pp. 213–245.
- [83] E. Laukli and R. Burkard, "Calibration/standardization of short-duration stimuli," *Seminars in Hearing* **36**, 3–10 (2015) doi: [10.1055/s-0034-1396923](https://doi.org/10.1055/s-0034-1396923).
- [84] S. Ewert, J. Verhey, and T. Dau, "Spectro-temporal processing in the envelope-frequency domain," *J. Acoust. Soc. Am.* **112**, 2921–2931 (2002) doi: [10.1121/1.1515735](https://doi.org/10.1121/1.1515735).
- [85] D. Schwartz, M. Morris, J. Spydel, C. Ten Brink, M. Grim, and J. Schwartz, "Influence of click polarity on the brainstem auditory evoked response (BAER) revisited," *Electroencephalogr. Clin. Neurophysiol.* **77**, 445–457 (1990) doi: [10.1016/0168-5597\(90\)90005-X](https://doi.org/10.1016/0168-5597(90)90005-X).
- [86] J. Undurraga, A. van Wieringen, R. Carlyon, O. Macherey, and J. Wouters, "Polarity effects on neural responses of the electrically stimulated auditory nerve at different cochlear sites," *Hear. Res.* **269**, 146–161 (2010) doi: [10.1016/j.heares.2010.06.017](https://doi.org/10.1016/j.heares.2010.06.017).
- [87] D. Ramekers, H. Versnel, S. Strahl, E. Smeets, S. Klis, and W. Grolman, "Auditory-nerve responses to varied inter-phase gap and phase duration of the electric pulse stimulus as predictors for neuronal degeneration," *J. Assoc. Res. Otolaryngol.* **15**, 187–202 (2014) doi: [10.1007/s10162-013-0440-x](https://doi.org/10.1007/s10162-013-0440-x).
- [88] F. Drakopoulos, D. Baby, and S. Verhulst, "A convolutional neural-network framework for modelling auditory sensory cells and synapses," *Commun. Biol.* **4**, 827 (2021) doi: [10.1038/s42003-021-02341-5](https://doi.org/10.1038/s42003-021-02341-5).
- [89] D. Baby, A. Van Den Broucke, and S. Verhulst, "A convolutional neural-network model of human cochlear mechanics and filter tuning for real-time applications," *Nat. Mach. Intell.* **3**, 134–143 (2020) doi: [10.1038/s42256-020-00286-8](https://doi.org/10.1038/s42256-020-00286-8).
- [90] F. Bianchi, L. Carney, T. Dau, and S. Santurette, "Effects of musical training and hearing loss on fundamental frequency discrimination and temporal fine structure processing: Psychophysics and modeling," *J. Assoc. Res. Otolaryngol.* **20**, 263–277 (2019) doi: [10.1007/s10162-018-00710-2](https://doi.org/10.1007/s10162-018-00710-2).
- [91] S. Verhulst, A. Jagadeesh, M. Mauermann, and F. Ernst, "Individual differences in auditory brainstem response wave characteristics: Relations to different aspects of peripheral hearing loss," *Trends in Hearing* **20**, 1–20 (2016) doi: [10.1177/2331216516672186](https://doi.org/10.1177/2331216516672186).
- [92] S. Verhulst, F. Ernst, M. Garrett, and V. Vasilkov, "Supra-threshold psychoacoustics and envelope-following response relations: normal-hearing, synaptopathy and cochlear gain loss," *Acta Acust. united Ac.* **104**, 800–803 (2018).
- [93] A. Osses Vecchi, F. Ernst, and S. Verhulst, "Hearing-impaired sound perception: What can we learn from a biophysical model of the human auditory periphery?," in *International Congress on Acoustics*, edited by M. Ochmann, M. Vorländer, and J. Fels, Aachen (2019), pp. 678–685, doi: [10.18154/rwth-conv-239764](https://doi.org/10.18154/rwth-conv-239764).
- [94] S. Jørgensen and T. Dau, "Predicting speech intelligibility based on the signal-to-noise envelope power ratio after modulation-frequency selective processing," *J. Acoust. Soc. Am.* **130**, 1475–1487 (2011) doi: [10.1121/1.3621502](https://doi.org/10.1121/1.3621502).
- [95] M. Jepsen and T. Dau, "Characterizing auditory processing and perception in individual listeners with sensorineural hearing loss," *J. Acoust. Soc. Am.* **129**, 262–281 (2011) doi: [10.1121/1.3518768](https://doi.org/10.1121/1.3518768).
- [96] M. Jepsen, S. Ewert, and T. Dau, "A computational model of human auditory signal processing and perception," *J. Acoust. Soc. Am.* **124**, 422–438 (2008) doi: [10.1121/1.2924135](https://doi.org/10.1121/1.2924135).
- [97] S. Ewert and T. Dau, "External and internal limitations in amplitude-modulation processing," *J. Acoust. Soc. Am.* **116**, 478–490 (2004) doi: [10.1121/1.1737399](https://doi.org/10.1121/1.1737399).
- [98] N. Wallaert, B. Moore, S. Ewert, and C. Lorenzi, "Sensorineural hearing loss enhances auditory sensitivity and temporal integration for amplitude modulation," *J. Acoust. Soc. Am.* **141**, 971–980 (2017) doi: [10.1121/1.4976080](https://doi.org/10.1121/1.4976080).
- [99] J. Breebaart, S. van de Par, and A. Kohlrausch, "Binaural processing model based on contralateral inhibition. I. Model structure," *J. Acoust. Soc. Am.* **110**, 1074–1088 (2001) doi: [10.1121/1.1383297](https://doi.org/10.1121/1.1383297).
- [100] J. van Dorp, D. de Vries, and A. Lindau, "Deriving content-specific measures of room acoustic perception using a binaural, nonlinear auditory model," *J. Acoust. Soc. Am.* **133**, 1572–1585 (2013) doi: [10.1121/1.4789357](https://doi.org/10.1121/1.4789357).
- [101] A. Osses Vecchi, A. Kohlrausch, W. Lachenmayr, and E. Mommertz, "Predicting the perceived reverberation in different room acoustic environments using a binaural model," *J. Acoust. Soc. Am.* **141**, EL381–EL387 (2017) doi: [10.1121/1.4979853](https://doi.org/10.1121/1.4979853).
- [102] A. Prokopiou, A. Moncada-Torres, J. Wouters, and T. Francart, "Functional modelling of interaural time difference discrimination in acoustical and electrical hearing," *J. Neural Eng.* **14**, 046021 (2017) doi: [10.1088/1741-2552/aa7075](https://doi.org/10.1088/1741-2552/aa7075).
- [103] E. Joosten, S. Shamma, C. Lorenzi, and P. Neri, "Dynamic reweighting of auditory modulation filters," *PLoS Comput. Biol.* **12**, e1005019 (2016) doi: [10.1371/journal.pcbi.1005019](https://doi.org/10.1371/journal.pcbi.1005019).
- [104] A. Nagathil, F. Göbel, A. Nelus, and I. Bruce, "Computationally efficient DNN-based approximation of an auditory model for applications in speech processing," in *Proc. of ICASSP* (2021), pp. 301–305, doi: [10.1109/ICASSP39728.2021.9413993](https://doi.org/10.1109/ICASSP39728.2021.9413993).
- [105] A. Mehta, P. Mehta, S. Anderson, B. MacKinnon, and A. Compston, "Etymology and the neuron(e)," *Brain* **143**, 374–379 (2020) doi: [10.1093/brain/awz367](https://doi.org/10.1093/brain/awz367).